ARMY RESEARCH LABORATORY

Modeling Nonlinear Electromechanical Behavior of Shocked Silicon Carbide

by John D. Clayton

ARL-RP-288 **January 2010**

A reprint from the *Journal of Applied Physics*,
Vol. 107, pp. 013520-1–013520-18, 2010.

NOTICES

Disclaimers

The findings in this report are not to be construed as an official Department of the Army position unless so designated by other authorized documents.

Citation of manufacturer's or trade names does not constitute an official endorsement or approval of the use thereof.

Destroy this report when it is no longer needed. Do not return it to the originator.

Army Research Laboratory
Aberdeen Proving Ground, MD 21005-5066

ARL-RP-288 **January 2010**

Modeling Nonlinear Electromechanical Behavior of Shocked Silicon Carbide

John D. Clayton
Weapons and Materials Research Directorate, ARL

A reprint from the *Journal of Applied Physics*,
Vol. 107, pp. 013520-1–013520-18, 2010.

REPORT DOCUMENTATION PAGE

Form Approved
OMB No. 0704-0188

1. REPORT DATE *(DD-MM-YYYY)*	2. REPORT TYPE	3. DATES COVERED (From - To)
January 2010	Reprint	1 January 2009–1 January 2010

4. TITLE AND SUBTITLE
Modeling Nonlinear Electromechanical Behavior of Shocked Silicon Carbide

5a. CONTRACT NUMBER

5b. GRANT NUMBER

5c. PROGRAM ELEMENT NUMBER

6. AUTHOR(S)
John D. Clayton

5d. PROJECT NUMBER
AH80

5e. TASK NUMBER

5f. WORK UNIT NUMBER

7. PERFORMING ORGANIZATION NAME(S) AND ADDRESS(ES)
U.S. Army Research Laboratory
ATTN: RDRL-WMT-D
Aberdeen Proving Ground, MD 21005-5066

8. PERFORMING ORGANIZATION REPORT NUMBER
ARL-RP-288

9. SPONSORING/MONITORING AGENCY NAME(S) AND ADDRESS(ES)

10. SPONSOR/MONITOR'S ACRONYM(S)

11. SPONSOR/MONITOR'S REPORT NUMBER(S)

12. DISTRIBUTION/AVAILABILITY STATEMENT
Approved for public release; distribution is unlimited.

13. SUPPLEMENTARY NOTES
A reprint from the *Journal of Applied Physics,* Vol. 107, pp. 013520-1–013520-18, 2010.

14. ABSTRACT

A model is developed for anisotropic ceramic crystals undergoing potentially large deformations that can occur under significant pressures or high temperatures. The model is applied to describe silicon carbide (SiC), with a focus on α-SiC, specifically hexagonal polytype 6*H*. Incorporated in the description are nonlinear anisotropic thermoelasticity, electrostriction, and piezoelectricity. The response of single crystals of α-SiC of various orientations subjected to one-dimensional shock loading is modeled for open- and short-circuit boundary conditions. The influences of elastic and electromechanical nonlinearity and anisotropy on the response to impact are quantified. For elastic axial compressive strains less than 0.1, piezoelectricity, electrostriction, and thermal expansion have a negligible influence on the mechanical (stress) response, but the influences of nonlinear elasticity (third-order elastic constants) and anisotropy are not insignificant. The model is extended to incorporate inelastic deformation and lattice defects. Addressed are Shockley partial dislocations on the basal plane and edge dislocation loops on the prism plane, dilatation from point defects and elastic fields of dislocation lines, and cleavage fracture. The results suggest that electric current generated in shock-loaded α-SiC crystals of certain orientations could affect the dislocation mobility and hence the yield strength at high pressure.

15. SUBJECT TERMS
silicon carbide, ceramic, elasticity, plasticity, defects

16. SECURITY CLASSIFICATION OF:			17. LIMITATION OF ABSTRACT	18. NUMBER OF PAGES	19a. NAME OF RESPONSIBLE PERSON
a. REPORT	b. ABSTRACT	c. THIS PAGE			John D. Clayton
Unclassified	Unclassified	Unclassified	UU	24	19b. TELEPHONE NUMBER (*Include area code*) 410-278-6146

Modeling nonlinear electromechanical behavior of shocked silicon carbide

J. D. Clayton[a)]
Impact Physics, US Army Research Laboratory, Aberdeen Proving Ground, Maryland 21005-5066, USA

(Received 31 July 2009; accepted 3 December 2009; published online 14 January 2010)

A model is developed for anisotropic ceramic crystals undergoing potentially large deformations that can occur under significant pressures or high temperatures. The model is applied to describe silicon carbide (SiC), with a focus on α-SiC, specifically hexagonal polytype 6*H*. Incorporated in the description are nonlinear anisotropic thermoelasticity, electrostriction, and piezoelectricity. The response of single crystals of α-SiC of various orientations subjected to one-dimensional shock loading is modeled for open- and short-circuit boundary conditions. The influences of elastic and electromechanical nonlinearity and anisotropy on the response to impact are quantified. For elastic axial compressive strains less than 0.1, piezoelectricity, electrostriction, and thermal expansion have a negligible influence on the mechanical (stress) response, but the influences of nonlinear elasticity (third-order elastic constants) and anisotropy are not insignificant. The model is extended to incorporate inelastic deformation and lattice defects. Addressed are Shockley partial dislocations on the basal plane and edge dislocation loops on the prism plane, dilatation from point defects and elastic fields of dislocation lines, and cleavage fracture. The results suggest that electric current generated in shock-loaded α-SiC crystals of certain orientations could affect the dislocation mobility and hence the yield strength at high pressure. [doi:10.1063/1.3277030]

I. INTRODUCTION

Silicon carbide is a ceramic material used in a number of structural, industrial, and electronics applications. Silicon carbide features high hardness[1] (Vickers hardness ~22 GPa), high melting point[2] (~3100 K), and high elastic stiffness[3] (bulk modulus ~220 GPa). High purity single crystals of SiC are of interest for use as anvils in high-pressure research and windows for optical spectroscopy and x-ray diffraction.[1,4] Silicon carbide is a semiconductor with a wide band gap[5] of 2.39–3.33 eV.

Over 200 structural polytypes of SiC crystals are known to exist.[6,7] A SiC polytype is represented by the number of Si–C double layers in its unit cell, with an appended *C*, *H*, or *R* denoting a cubic, hexagonal, or rhombohedral crystal system. Cubic polytypes are classified as β-SiC; hexagonal and rhombohedral polytypes are labeled α-SiC. The common cubic polytype is 3*C*-SiC, exhibiting the sphalerite or zinc blende crystal structure. Technologically relevant polytypes of hexagonal SiC include 2*H* (wurtzite structure), 4*H*, and 6*H*, while common rhombohedral polytypes include 9*R*, 12*R*, and 15*R*. Hexagonal α polytype 6*H*-SiC is the focus of the present investigation; crystals of 6*H*-SiC are often referred to as moissanite. Industrial polycrystalline ceramics such as SiC–B and SiC–N are thought to consist primarily of 6*H*-SiC,[8–10] though fractions of other polytypes may be present.

Polytype 6*H*-SiC is noncentrosymmetric, piezoelectric, and can exhibit spontaneous polarity.[11] Phase transformations between cubic and hexagonal polytypes at ambient pressure occur at temperatures in excess of 1800 K.[12] Phase transformations at lower ambient temperatures are thought to occur at very high pressures on the order of 100 GPa,[13] though fractional increases in 6*H*-SiC grains relative to other polytypes have been observed to occur at somewhat lower compressive stresses (~19–32 GPa) in polycrystalline SiC subject to ballistic impact.[10] Basal slip of edge dislocations in hexagonal polytypes is the dominant mechanism of plastic deformation,[5] with dislocation mobility dependent on temperature and electric current or bias voltage.[14,15] Shockley partial dislocations bordering intrinsic stacking faults are thought to be most relevant in hexagonal SiC,[5,16] with mobility of leading partials exceeding that of trailing partials at low temperatures,[17] supporting a tendency for plasticity to be accompanied by generation of large numbers of stacking faults. Twinning observed in β-SiC (Ref. 18) does not appear to be an important mechanism in hexagonal polytypes, except at high temperatures and pressures wherein phase transformations occur. Point defects such as Si and C vacancies[6,10] and interstitials[19] may affect mechanical and electrical properties. Primary cleavage planes are of basal and prismatic orientations; single crystals of hexagonal SiC have been reported less resistant to fracture during indentation experiments than their polycrystalline counterparts.[20]

The present work addresses nonlinear behavior of single crystals of 6*H*-SiC. Models incorporating geometric nonlinearity (finite deformations) and material nonlinearity (higher-order elastic constants) are needed to interpret results of shock physics experiments on anisotropic ceramic single crystals.[21,22] Because 6*H*-SiC crystals are piezoelectric, electromechanical behavior should be addressed.[23–25] The importance, or lack thereof, of electromechanical forces (e.g., piezoelectricity and electrostriction) on the response of single crystals of α-SiC deformed in planar impact under various electrical boundary conditions, to the author's knowledge, has remained undocumented prior to the present study.

[a)]Electronic mail: jclayton@arl.army.mil.

The results of shock physics experiments (e.g., plate impact or explosive loading) on single crystals of 6*H*-SiC have not been reported in literature, to the author's knowledge. Experimental measurements of anisotropic second-order elastic constants of 6*H*-SiC are available,[3,26] but pressure derivatives of second-order coefficients have only been estimated theoretically.[27] Dielectric permittivity, piezoelectric coefficients, and thermal conductivity are available from experimental and/or quantum mechanical studies.[28–36] Shock physics experiments on polycrystals of α-SiC have indicated that SiC maintains significant strength above the Hugoniot elastic limit (HEL) and suggest that deformation by dislocation generation and motion may occur in SiC under high confining pressures, even near room temperature.[8,13,37] Large dislocation densities have been measured in α-SiC subjected to explosive shock loading.[2] The occurrence of plasticity in SiC has been noted in indentation experiments[38] and atomistic simulations.[39]

Zhang *et al.*[40–42] developed a crystal plasticity model for hexagonal SiC incorporating dislocation glide on basal planes, possible slip on prism planes, and failure at amorphous regions in the vicinity of grain boundaries. Computational studies of Zhang *et al.*[42] suggest that basal slip is more viable than fracture when considering longitudinal and lateral stress profiles measured in impact experiments on polycrystals. Nontextured polycrystals were addressed; hence, electromechanical interactions were omitted in numerical simulations.[40–42] Isolated slip of leading partial dislocations was not considered explicitly, nor were temperature effects such as adiabatic heating, thermal expansion, and thermally enhanced dislocation mobility. The present work will show that, in the elastic regime, omission of thermal effects is a reasonable assumption, though it may not always be in the plastic regime if dissipated energy from dislocation glide is substantial.

When considering polycrystals (randomly oriented grains) whose overall response can be idealized as macroscopically isotropic and hence centrosymmetric, macroscopic piezoelectric effects will not be observed; thus, the choice of electrical boundary conditions (e.g., open versus closed circuit) would not be expected to affect the global mechanical response or interpretation of mechanical data such as stresses and pressures from static or impact experiments. However, electromechanical effects could be important for single crystals. Recent interest has emerged in high-pressure behavior of single crystals of α-SiC for use in anvil cells or window materials in high-pressure research.[1,4] It is hoped that the analysis, results, and compiled/computed properties for α-SiC in the present paper may motivate and guide future experiments on single crystals. The present treatment of plasticity and lattice defects, whose structure and mobility can be influenced by electrical conditions and hence electromechanical properties, may also be of interest for semiconductor applications.[5,14–17]

This paper is organized as follows. Section II describes a general model for nonlinear electromechanical behavior of noncentrosymmetric elastic dielectric single crystals. The model incorporates principles from nonlinear electromechanics under the quasielectrostatic approximation.[25,43–45] In Sec. III, the model is specialized to describe single crystals of α-SiC. Section IV describes model predictions of the response of oriented single crystals to one-dimensional shock loading. Section V extends the model to incorporate plastic slip[22,46] and influences of point and line defects,[47,48] and assesses predictions of material behavior to the extent permitted by the availability of experimental data. Vectors and tensors are expressed in indicial notation in Cartesian coordinates, with summation implied over repeated subscripted indices. Superposed -1 and $\bullet$ denote inversion and the material time derivative, respectively.

II. NONLINEAR MODEL FOR ELASTIC DIELECTRICS

A. Kinematics

The reference configuration of a body is denoted B_0, and the spatial or current configuration of the body is denoted B_t. Let $x_a = x_a(X_A, t)$ denote spatial coordinates that depend on reference coordinates X_A of a material particle and time t. In regions where spatial positions are differentiable, the deformation gradient and its inverse are

$$F_{aA}(X_A,t) = \partial_A x_a, \quad F^{-1}_{Aa}(x_a,t) = \partial_a X_A, \tag{1}$$

where $\partial_A(\cdot) = \partial(\cdot)/\partial X_A = F_{aA}\partial_a(\cdot)$ and $\partial_a(\cdot) = \partial(\cdot)/\partial x_a = F^{-1}_{Aa}\partial_A(\cdot)$. The spatial velocity gradient is

$$L_{ab} = \partial_b \dot{x}_a = \partial_b v_a = \dot{F}_{aA}F^{-1}_{Ab}. \tag{2}$$

Referential and spatial mass densities ρ_0 and ρ are related by

$$\rho_0 = \rho J, \quad \dot{\rho} = -\rho \dot{J} J^{-1} = -\rho \partial_a v_a, \tag{3}$$

where $J = \det(F_{aA})$. Piola's identities for the Jacobian determinant and its inverse are

$$\partial_A(JF^{-1}_{Aa}) = 0, \quad \partial_a(J^{-1}F_{aA}) = 0. \tag{4}$$

Symmetric tensors of finite deformation and strain are introduced, with δ_{AB} Kronecker's delta

$$C_{AB} = F_{aA}F_{aB}, \quad C^{-1}_{AB} = F^{-1}_{Aa}F^{-1}_{Ba}, \quad 2E_{AB} = C_{AB} - \delta_{AB}. \tag{5}$$

B. Electromechanics

The present description of dielectric solids follows a quasielectrostatic approximation.[25,43–45] In this treatment, deemed appropriate for shock physics experiments on dielectric crystals,[23,24,49] finite material velocity and acceleration are considered, but electromagnetic waves (e.g., optical phenomena) are not. The treatment is restricted to nonmagnetic materials with particle velocities small compared to light speed in vacuum. Appropriate local, spatial forms of Maxwell's equations are

$$\varepsilon_{abc}\partial_b \hat{e}_c = 0, \quad \partial_a \hat{d}_a = \hat{\rho}, \quad \partial \hat{d}_a/\partial t = -\hat{j}_a, \quad \hat{b}_{a,a} = 0, \tag{6}$$

with $\hat{e}_a$ the electric field, $\hat{d}_a$ the electric displacement, and $\hat{\rho}$ the free charge density. Electric current density is $\hat{j}_a$, and $\hat{b}_a$ is the magnetic flux density. The permutation tensor is ε_{abc}. Relation (6) applies where electric field and electric displacement are differentiable; jump conditions over an oriented surface are

$$\varepsilon_{abc}[\![\hat{e}_c]\!]n_b = 0, \quad [\![\hat{d}_a]\!]n_a = \hat{\sigma}, \tag{7}$$

where $\hat{\sigma}$ is the surface charge density, n_a is the unit normal pointing from inside to outside a surface, and jump $[\![a]\!]=a^+ - a^-$ for quantity a, where superscripts + and − correspond to the limiting value of a outside and inside the surface. Denoting by $\hat{\phi}$ the electrostatic potential, the electric field satisfies

$$\hat{e}_a = -\partial_a \hat{\phi}. \tag{8}$$

Electric displacement, electric field, and spatial polarization $\hat{p}_a$ are related by

$$\hat{d}_a = \varepsilon_0 \hat{e}_a + \hat{p}_a, \tag{9}$$

with ε_0 the vacuum permittivity. "Material" or "Lagrangian" measures of electric field, electric displacement, electric polarization, and free charge density in the reference configuration are[25,45,50,51]

$$\hat{E}_A = F_{aA}\hat{e}_a, \quad \hat{D}_A = JF^{-1}_{Aa}\hat{d}_a, \quad \hat{P}_A = F_{aA}\hat{p}_a, \quad \hat{\rho}_0 = J\hat{\rho}. \tag{10}$$

From Eqs. (1), (4), and (8)–(10), material electrostatic quantities obey

$$\hat{E}_A = -\partial_A \hat{\phi}, \quad \partial_A \hat{D}_A = \hat{\rho}_0, \quad \hat{D}_A = JC^{-1}_{AB}(\varepsilon_0 \hat{E}_B + \hat{P}_B). \tag{11}$$

The local balance of linear momentum in regions where field variables are suitably differentiable is

$$\partial_b T_{ab} + \bar{b}_a = \rho \dot{v}_a, \tag{12}$$

where $\bar{b}_a$ is the mechanical body force per unit spatial volume and $T_{ab}=\sigma_{ab}+\hat{\tau}_{ab}$ is the total stress tensor that is the sum of mechanical or Cauchy stress σ_{ab} and Maxwell stress $\hat{\tau}_{ab}$. Maxwell's stress tensor is[52,53]

$$\hat{\tau}_{ab} = \hat{e}_a\hat{p}_b + \varepsilon_0 \hat{e}_a\hat{e}_b - (\varepsilon_0/2)(\hat{e}_c\hat{e}_c)\delta_{ab}. \tag{13}$$

The local balance of angular momentum is

$$T_{ab} = T_{ba}. \tag{14}$$

Maxwell's stress need not be continuous across coherent interfaces. Traction boundary conditions are

$$T_a = t^+_a = t^-_a - [\![\hat{\tau}_{ab}]\!]n_b, \quad t^{\pm}_a = \sigma^{\pm}_{ab} n_b. \tag{15}$$

In the classical linear theory of piezoelectricity,[54] Maxwell stress (13) is omitted and $\sigma_{ab}=\sigma_{ba}$.

C. Thermodynamics

The local form of the balance of energy for a dielectric in the current configuration is[45]

$$\rho \dot{e} = \sigma_{ab}L_{ab} - \partial_a q_a + \rho r + \hat{e}_a \dot{\hat{p}}_a, \tag{16}$$

where e is the internal energy per unit mass, q_a is the heat flux, and r is the scalar heat source. A local form of the dissipation inequality is[45,53]

$$\rho\theta\dot{\eta} - \rho r + \partial_a q_a - \theta^{-1} q_a \partial_a \theta \geq 0, \tag{17}$$

with η the entropy and θ the absolute temperature. Defining the Helmholtz free energy as $\psi=e-\theta\eta$ and using Eqs. (16) and (17) result to

$$\sigma_{ab}L_{ab} + \hat{e}_a\dot{\hat{p}}_a - \rho(\dot{\psi} + \dot{\theta}\eta) - \theta^{-1} q_a \partial_a \theta \geq 0. \tag{18}$$

For an elastic dielectric, the free energy is assumed to exhibit the general functional form

$$\psi = \psi(E_{AB}, \hat{P}_A, \theta), \tag{19}$$

where strain E_{AB} is defined in Eq. (5) and referential polarization $\hat{P}_A$ is defined in Eq. (10). Following standard thermodynamic procedures,[25,44,53] the following constitutive laws are obtained:[45]

$$\eta = -\partial\psi/\partial\theta, \tag{20}$$

$$\Sigma_{AB} = JF^{-1}_{Aa}\sigma_{ab}F^{-1}_{Bb} = \rho_0 \frac{\partial \psi}{\partial E_{AB}} + JC^{-1}_{AC}\hat{P}_C C^{-1}_{BD}\hat{E}_D, \tag{21}$$

$$\hat{e}_a = F_{aA}\rho \frac{\partial \psi}{\partial \hat{P}_A}, \quad \hat{E}_A = J^{-1}C_{AB}\rho_0 \frac{\partial \psi}{\partial \hat{P}_B}. \tag{22}$$

The second Piola–Kirchhoff stress, referred to in shock physics literature[23,24,50] as the thermodynamic tension, is Σ_{AB}. Assigning reference heat flux Q_A with Fourier conduction law

$$Q_A = JF^{-1}_{Aa}q_a = -K_{AB}\partial_B\theta, \tag{23}$$

where K_{AB} is the thermal conductivity, and using Eqs. (20)–(22), dissipation inequality (18) reduces to

$$(J\theta)^{-1}K_{AB}\partial_A\theta\partial_B\theta \geq 0. \tag{24}$$

Introducing the specific heat c per unit mass at fixed polarization and fixed strain, thermal stress coefficients at fixed polarization β_{AB}, and pyroelectric coefficients at fixed strain χ_A,

$$c = \frac{\partial e}{\partial \theta} = -\theta \frac{\partial^2 \psi}{\partial \theta^2}, \quad \beta_{AB} = -\rho_0 \frac{\partial^2 \psi}{\partial\theta\,\partial E_{AB}}, \quad \chi_A = -\rho_0 \frac{\partial^2 \psi}{\partial\theta\,\partial \hat{P}_A}, \tag{25}$$

and using Eqs. (4) and (19), balance of energy (16) can be expressed as a rate equation for the temperature[55]

$$\rho_0 c\,\dot{\theta} = \partial_A(K_{AB}\partial_B\theta) + \rho_0 r - \theta(\beta_{AB}\dot{E}_{AB} + \chi_A \dot{\hat{P}}_A). \tag{26}$$

III. 6*H*-SILICON CARBIDE: STRUCTURE AND PHYSICAL PROPERTIES

A. Crystal structure

Structures of SiC polytypes are described by Wyckoff.[7] Anisotropic physical properties can be explained in terms of fractions of hexagonal and cubic layers in a given polytype.[31,56] Silicon carbide of polytype 6*H* belongs to space group $C_{6v}{}^4$ ($C6mc$) and point group $6mm$, the latter in

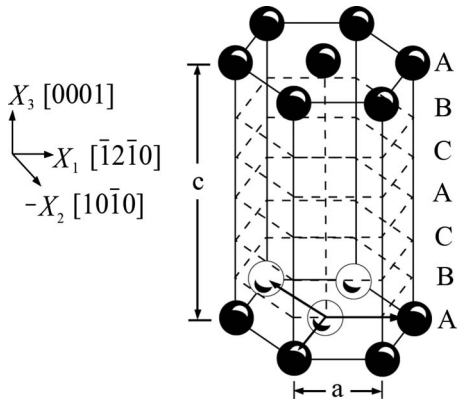

FIG. 1. Structure of 6*H*-SiC and crystallographic coordinate system.

Laue group HI and the dihexagonal pyramidal class.[26,50] The stacking sequence of Si or C layers in the [0001] direction is *ABCACBABCACB*…, meaning six layers each of Si and C comprise a conventional unit cell (Fig. 1). The lattice parameters at room temperature and atmospheric pressure are c =1.512 nm and a=0.308 nm,[36] leading to cell volume $\sqrt{3}a^2c/2=0.124$ nm^3 and average atomic volume $\Omega_0=\sqrt{3}a^2c/24=0.0103$ nm^3.

B. Thermoelectromechanical properties

A specific form of free energy (19) is written, on a per unit reference volume basis, as

$$\rho_0\psi=(1/2)C_{ABCD}E_{AB}E_{CD}+(1/6)C_{ABCDEF}E_{AB}E_{CD}E_{EF}+(1/2)\Lambda_{AB}\hat{P}_A\hat{P}_B+\Delta_{ABC}\hat{P}_AE_{BC}+(1/2)\Upsilon_{ABCD}\hat{P}_A\hat{P}_BE_{CD}-\beta_{AB}E_{AB}\Delta\theta-\rho_0c\theta\ln(\theta/\theta_0). \quad (27)$$

Temperature change from the reference state is $\Delta\theta=\theta-\theta_0$. Consider a coordinate system with an orthonormal basis $(\mathbf{i},\mathbf{j},\mathbf{k})$, where $\mathbf{i}$ is along basis vector $\mathbf{a}$ and direction $[\bar{1}2\bar{1}0]$, $\mathbf{j}$ is along $[\bar{1}010]$, and $\mathbf{k}$ is along $\mathbf{c}$ and direction [0001], following the IRE standard[54] and Fig. 1. Properties corresponding to Eq. (27) in this coordinate system are listed in Tables I and II. Voigt's notation,[50] with symmetric indicial pairs 11→1, 22→2, 33→3, 23→4, 13→5, and 12→6, is used in the tables for some coefficients. Energy (27) is written in a continuum sense and is representative of a volume of crystal containing a large number of unit cells. Inner displacements of Si or C atoms belonging to different primitive sublattices that affect the measured properties[19,35] are implicitly included in material coefficients entering Eq. (27).

TABLE I. Thermophysical properties.

Parameter	Value	Definition	Ref.
ρ_0	3210 kg/m^3	Mass density	28
c_p	652 J/kg K	Isobaric specific heat	63
α_{11}	3.4×10^{-6}/K	Thermal expansion coefficients	31
α_{33}	3.2×10^{-6}/K		
K_{11}	390 W/mK	Thermal conductivity	30
K_{33}	370 W/mK		
Θ_D	1200 K	Debye temperature	28
Θ_M	3375 K	Melting temperature	2

TABLE II. Elastic, piezoelectric, and dielectric properties.

Parameter	Value	Definition	Ref.
C_{11}	501±6 GPa	Second-order elastic constants	3
C_{12}	112±5 GPa		
C_{13}	52±9 GPa		
C_{33}	549±3 GPa		
C_{44}	161±4 GPa		
$\partial C_{11}/\partial p$	3.8	Pressure derivatives of second-order elastic coefficients	27
$\partial C_{12}/\partial p$	4.0		
$\partial C_{13}/\partial p$	4.0		
$\partial C_{33}/\partial p$	3.8		
$\partial C_{44}/\partial p$	−0.2		
μ	194 GPa	Isotropic elastic constants	5
ν	0.161		5
B	222 GPa		Equation (30)
	230 GPa		59
$B'=\partial B/\partial p$	4.0	Pressure derivative of bulk modulus	59
	3.1±0.3		60
	3.9		Equation (30)
	2.5		$B'=2\Gamma+1/3$ (Ref. 61)
$\mu'=\partial\mu/\partial p$	3.4	Pressure derivative of shear modulus	Isotropic, fixed ν
e_{15}	−0.198 C/m^2	Piezoelectric constants	35
e_{31}	−0.200 C/m^2		
e_{33}	0.398 C/m^2		
ε_{11}	9.66	Static dielectric permittivity	29
ε_{33}	10.03		
$\partial\varepsilon_{11}/\partial p$	−0.0218/GPa	Pressure derivatives of permittivity	34
$\partial\varepsilon_{33}/\partial p$	−0.0232/GPa		

Isothermal second- and third-order elastic constants at fixed polarization in full index notation are

$$C_{ABCD}=\rho_0\left.\frac{\partial^2\psi}{\partial E_{AB}\,\partial E_{CD}}\right|_{B_0},\quad C_{ABCDEF}=\rho_0\left.\frac{\partial^3\psi}{\partial E_{AB}\,\partial E_{CD}\,\partial E_{EF}}\right|_{B_0}, \quad (28)$$

where partial derivatives are evaluated at a fixed reference state B_0 characterized by

$$\{B_0{:}\rho=\rho_0,\quad F_{aA}=\delta_{aA},\quad E_{AB}=0,\quad \hat{P}_A=0,\quad \theta=\theta_0\}. \quad (29)$$

Hexagonal crystals of Laue group HI exhibit five independent second-order and ten independent third-order elastic constants.[50] The former are available from experiments;[3,26] the latter apparently are not. However, pressure derivatives of second-order elastic coefficients are known from an atomic force model;[27,57] these are listed in Table II. Isother-

mal bulk modulus B at the reference state is defined as[58]

$$B = \left(\rho\frac{\partial p}{\partial \rho}\right)\Big|_{B_0} = -\left(J\frac{\partial p}{\partial J}\right)\Big|_{B_0} = \frac{C_{33}(C_{11}+C_{12})-2(C_{13})^2}{C_{11}+C_{12}-4C_{13}+2C_{33}}, \tag{30}$$

where C_{AB} are second-order elastic constants of the first of Eq. (28) written in Voigt's notation. Third-order elastic constants can be approximated from pressure derivatives of second-order coefficients via

$$C_{ABCDEF} = -\frac{B}{3}\left(\frac{\partial C_{ABCD}}{\partial p}\Big|_{B_0}\delta_{EF} + \frac{\partial C_{CDEF}}{\partial p}\Big|_{B_0}\delta_{AB} + \frac{\partial C_{EFAB}}{\partial p}\Big|_{B_0}\delta_{CD}\right), \tag{31}$$

an approximation that omits dependence of elastic coefficients on shear strains. Isotropic values[5] (Voigt averages) of shear modulus μ and Poisson's ratio ν are listed in Table II for polycrystalline 6H-SiC. The temperature dependence of elastic coefficients of SiC is thought to be weak[56] for $\theta < 800$ K and is omitted in Eq. (27). The pressure derivatives of isotropic elastic coefficients at the reference state are also listed, following polycrystalline experiments[59,60] or theoretical predictions.[61]

Isothermal second-order dielectric coefficients and piezoelectric coefficients are, respectively,

$$\Lambda_{AB} = \rho_0 \left.\frac{\partial^2\psi}{\partial\hat{P}_A\,\partial\hat{P}_B}\right|_{B_0}, \quad \Delta_{ABC} = \rho_0 \left.\frac{\partial^2\psi}{\partial\hat{P}_A\,\partial E_{BC}}\right|_{B_0}. \tag{32}$$

For the crystal class of hexagonal SiC, the first of Eq. (32) consists of two independent components (Λ_{11} and Λ_{33}) while the second consists of three ($\Delta_{113}=\Delta_{15}$, $\Delta_{311}=\Delta_{31}$, and $\Delta_{333}=\Delta_{33}$ in full and Voigt notations, respectively). Usual dielectric constants (dimensionless isothermal permittivity at constant strain) are

$$\varepsilon_{AB} = \left.\frac{1}{\varepsilon_0}\frac{\partial\hat{D}_A}{\partial\hat{E}_B}\right|_{B_0} = \delta_{AB} + \varepsilon_0^{-1}\Lambda_{AB}^{-1}, \quad \Lambda_{AB} = \varepsilon_0^{-1}(\varepsilon_{AB} - \delta_{AB})^{-1}. \tag{33}$$

The relationships between usual isothermal piezoelectric coefficients e_{ABC} defined as energy derivatives with respect to electric field[25,35,43,54] and those in Eq. (32) are[62]

$$e_{ABC} = -\left.\frac{\partial\Sigma_{BC}}{\partial\hat{E}_A}\right|_{\theta} = -\Lambda_{AD}^{-1}\Delta_{DBC}, \quad \Delta_{ABC} = -\Lambda_{AD}e_{DBC}. \tag{34}$$

Pyroelectricity is not considered. Third-order electromechanical (electrostriction) coefficients are

$$\Upsilon_{ABCD} = \rho_0 \left.\frac{\partial^3\psi}{\partial\hat{P}_A\,\partial\hat{P}_B\,\partial E_{CD}}\right|_{B_0}, \tag{35}$$

and are related to pressure derivatives of permittivity as follows if dependence on shear strain is omitted:

$$\Upsilon_{ABEE} = \left.\frac{3B\varepsilon_0}{4}\frac{\partial\varepsilon_{CD}}{\partial p}\right|_{B_0}\Lambda_{AC}\Lambda_{BD} + \varepsilon_0\Lambda_{AC}\Lambda_{BC} - \Lambda_{AB}. \tag{36}$$

The number of independent coefficients of Υ_{ABCD} is six for the crystal class of 6H-SiC.[50] The variation of permittivity with pressure is known,[34] providing two (Υ_{11} and Υ_{33}) of the six coefficients via

$$\Upsilon_{ABCD} = \Upsilon_{AB}\delta_{CD}, \quad \Upsilon_{ABCD}\delta_{CD} = 3\Upsilon_{AB}. \tag{37}$$

Second-order thermal stress coefficients at constant polarization are

$$\beta_{AB}|_{B_0} = -\rho_0 \left.\frac{\partial^2\psi}{\partial\theta\,\partial E_{AB}}\right|_{B_0} = C_{ABCD}\alpha_{CD}, \tag{38}$$

where α_{CD} is the tensor of thermal expansion at the reference state with independent coefficients α_{11} and α_{33}. Gruneisen numbers and scalar Gruneisen parameter are

$$\Gamma_{AB} = \beta_{AB}/(\rho_0 c), \quad \Gamma = \alpha_{AA}B/(\rho_0 c), \tag{39}$$

where the specific heat at constant volume in the reference state is

$$c|_{B_0} = -(\theta\partial^2\psi/\partial\theta^2)|_{B_0} = c_p - (\alpha_{AA})^2 B\theta_0/\rho_0, \tag{40}$$

with c_p the isobaric specific heat. In Eq. (27), a constant specific heat is used for small temperature variations from the reference state.[63] Thermal conductivities (K_{11} and K_{33}) listed in Table I are values at room temperature.[30] At room temperature, $c/c_p = 0.997$. Since the ratio of isothermal to isentropic bulk modulus $B/B^\eta = c/c_p \approx 1.0$ for $\theta \leq 1500$ K,[33] differences between isentropic and isothermal bulk moduli are omitted in regime $\theta \approx \theta_0 < \Theta_D$. The differences between isentropic and isothermal second-order elastic constants are[50]

$$C_{ABCD}^{\eta} - C_{ABCD} = (\theta_0/c)\beta_{AB}\beta_{CD}. \tag{41}$$

Nonzero differences in Eq. (41) for 6H-SiC in Voigt's notation, $C_{11}^{\eta} - C_{11} = 0.76$ GPa, $C_{33}^{\eta} - C_{33} = 0.63$ GPa, and $C_{13}^{\eta} - C_{13} = 0.69$ GPa, are smaller than the margins of experimental uncertainty for measured isentropic second-order elastic constants[3] and hence are omitted.

The following differences exist among isothermal elastic constants measured at fixed polarization C_{ABCD}, at fixed electric field $C_{ABCD}^{\hat{E}}$, and at fixed electric displacement $C_{ABCD}^{\hat{D}}$ as follows:[50,62]

$$C_{ABCD}^{\hat{E}} - C_{ABCD} = -\Delta_{EAB}\Lambda_{EF}^{-1}\Delta_{FCD}, \quad C_{ABCD}^{\hat{E}} - C_{ABCD}^{\hat{D}} = -e_{EAB}\varepsilon_0^{-1}\varepsilon_{EF}^{-1}e_{FCD}. \tag{42}$$

The largest differences among nonzero elastic constants are $C_{33}^{\hat{E}} - C_{33} = -1.98$ GPa, $C_{33}^{\hat{E}} - C_{33}^{\hat{D}} = -1.78$ GPa, and $C_{33}^{\hat{D}} - C_{33} = -0.20$ GPa. Since these differences are small and are within limits of experimental accuracy,[3] they are omitted in

the forthcoming analysis. The properties listed in Tables I and II correspond to 6*H*-SiC, with two exceptions. The pressure derivatives of elastic coefficients in Eq. (31) correspond to 2*H*-SiC,[27] and the pressure derivatives of permittivity in Eq. (36) correspond to 4*H*-SiC,[34] since the values for 6*H*-SiC were not available. Such pressure derivatives are evaluated at reference state (29).

Using Eq. (27) and the thermodynamic results of Sec. II C, useful algebraic expressions can be derived. The material electric field in terms of strain and polarization is, from Eq. (22),

$$\hat{E}_A = J^{-1}C_{AB}\Delta_{BCD}E_{CD} + J^{-1}C_{AB}(\Lambda_{BC} + \Upsilon_{BCDE}E_{DE})\hat{P}_C. \tag{43}$$

The material electric displacement in terms of strain and polarization is then obtained from Eq. (11) as

$$\hat{D}_A = (\varepsilon_0\Lambda_{AB} + JC^{-1}_{AB} + \varepsilon_0\Upsilon_{ABEF}E_{EF})\hat{P}_B + \varepsilon_0\Delta_{ADE}E_{DE}. \tag{44}$$

Inverting Eq. (43), the material polarization in terms of strain and electric field is

$$\hat{P}_C = (\Lambda_{BC} + \Upsilon_{BCDE}E_{DE})^{-1}(JC^{-1}_{BA}\hat{E}_A - \Delta_{BFG}E_{FG}), \tag{45}$$

or in terms of strain and electric displacement, after inverting Eq. (44),

$$\hat{P}_B = (\varepsilon_0\Lambda_{AB} + JC^{-1}_{AB} + \varepsilon_0\Upsilon_{ABEF}E_{EF})^{-1}(\hat{D}_A - \varepsilon_0\Delta_{ADE}E_{DE}). \tag{46}$$

The electric displacement in terms of strain and electric field is, combining Eqs. (44) and (46),

$$\hat{D}_A = \bar{\varepsilon}_{AD}\hat{E}_D + \bar{e}_{ADE}E_{DE} = \bar{\varepsilon}_{AD}\hat{E}_D + \bar{P}_A, \tag{47}$$

where $\bar{\varepsilon}_{AD}$ is the strain-dependent permittivity, $\bar{e}_{ADE}$ are the strain-dependent piezoelectric coefficients, and $\bar{P}_A$ is the strain-induced part of the polarization that does not depend on electric field. The thermodynamic tension of Eq. (21) is, using Eqs. (27) and (37),

$$\begin{aligned}\Sigma_{AB} = {} & C_{ABCD}E_{CD} + (1/2)C_{ABCDEF}E_{CD}E_{EF} \\ & + (1/2)\Upsilon_{CD}\delta_{AB}\hat{P}_C\hat{P}_D + \Delta_{CAB}\hat{P}_C - \beta_{AB}\Delta\theta \\ & + C^{-1}_{AC}\hat{P}_C(\Lambda_{BD}\hat{P}_D + \Delta_{BDE}E_{DE} + \Upsilon_{BD}\hat{P}_D E_{FF}).\end{aligned} \tag{48}$$

The symmetric total stress in momentum balance (12) is obtained by combining Eqs. (43) and (48) in the sum

$$\begin{aligned}T_{ab} = {} & J^{-1}F_{aA}\Sigma_{AB}F_{bB} + F^{-1}_{Aa}(\hat{E}_A\hat{P}_B + \varepsilon_0\hat{E}_A\hat{E}_B)F^{-1}_{Bb} \\ & - (\varepsilon_0/2)C^{-1}_{AB}\hat{E}_A\hat{E}_B\delta_{ab}.\end{aligned} \tag{49}$$

IV. SHOCK RESPONSE OF 6*H*-SIC

A. One-dimensional analysis

Consider a disk of piezoelectric crystal of initial thickness l_0, as shown in Fig. 2. The disk is subjected to planar impact along face $X=0$, while face $X=l_0$ remains fixed until the arrival of the stress wave at $t=t_0$. Impact loading imparts

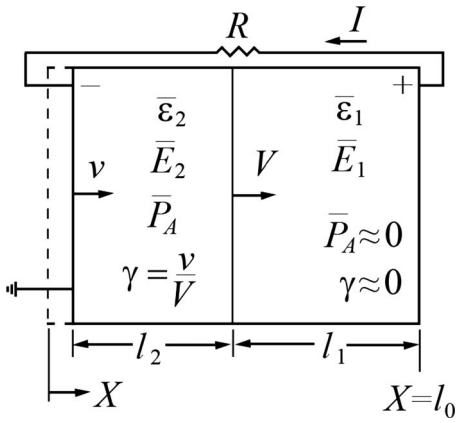

FIG. 2. One-dimensional shock-loaded piezoelectric disk of initial thickness l_0 (Refs. 23 and 24). Shock wave travels from left to right at velocity V; particle velocity is v. Wave divides disk into a shocked region of length $l_2(t)$ and an unshocked region of length $l_1(t)$. Effective dielectric permittivity and material electric field in regions 1 and 2 are $[\bar{\varepsilon}_1, \bar{E}_1(t)]$ and $[\bar{\varepsilon}_2(t), \bar{E}_2(t)]$. Compressive strain is γ, and $\bar{P}_A$ are strain-induced components of polarization. Measured displacement current is $I(t)$, with R the electrical resistance.

face $X=0$ with particle velocity v, and the absolute velocity of the shock referred to the reference configuration is V. Both v and V are assumed constant in time and one dimensional. Considered is the response for the first transit of the shock through the disk; i.e., $0 \le t \le t_0$.

1. Governing equations

In one dimension, denote the material coordinate by X and spatial coordinate by $x(X,t)$. Displacement is $u=x-X$. In region 2 (i.e., behind the shock) deformation gradient F and velocity v satisfy

$$F = \partial x/\partial X = 1 + \partial u/\partial X, \quad v = \partial x/\partial t = \partial u/\partial t. \tag{50}$$

Jacobian in Eq. (3) and its inverse are simply

$$J = F, \quad J^{-1} = F^{-1}. \tag{51}$$

In a material initially unstrained and at rest, shock velocity $V>0$ and particle velocity $0<v<V$ are related by the continuity equations[23,49,50]

$$v = -V(\partial u/\partial X) = V\gamma, \quad \gamma = v/V = -\partial u/\partial X = 1 - F. \tag{52}$$

The X-component, and the only nonzero component, of finite strain measure (5) is

$$E = (F^2 - 1)/2 = (\partial u/\partial X)^2/2 + \partial u/\partial X = \gamma^2/2 - \gamma. \tag{53}$$

The components of Lagrangian electric field and electric displacement of Eq. (10) in the X-direction are

$$\bar{E} = F\hat{e} = -\partial\hat{\phi}/\partial X, \quad \bar{D} = JF^{-1}\hat{d} = \hat{d}. \tag{54}$$

Local governing equations of Sec. II apply within regions 1 and 2 but not across the shock. In the one-dimensional case, global balance laws are written as follows.[43,49] Let X_1 and X_2 denote the coordinates of any two material points. The specimen is idealized as a perfect dielectric with no free charges [$\hat{\rho}_0=0$ in Eq. (11)], and body forces besides those associated with Maxwell's stress are absent [$\bar{b}_a=0$ in Eq. (12)]. The

global balance of linear momentum is

$$T(X_2,t) - T(X_1,t) = \frac{d}{dt}\int_{X_1}^{X_2} \rho_0 v dX, \tag{55}$$

where $T(X,t)$ is the component of the total stress of Eqs. (12) and (49) normal to the X-direction. The one-dimensional form of Gauss's law is

$$\bar{D}(X_2,t) - \bar{D}(X_1,t) = 0. \tag{56}$$

For all regions of the specimen except across the shock, the local forms of Eqs. (55) and (56) are

$$\partial T/\partial X = \rho_0(\partial v/\partial t), \quad \partial \bar{D}/\partial X = J(\partial \bar{D}/\partial x) = 0. \tag{57}$$

The third of Maxwell's relations in Eq. (6) becomes, in one dimension,

$$I/A = -\hat{j} = \partial \hat{d}/\partial t = d\bar{D}/dt, \tag{58}$$

where $I(t)$ is the electric displacement current and A is the area of the collecting electrode at $X=l_0$. The gradient of Eq. (58), with Eq. (57), leads to the independence of current density with position; i.e.,

$$\partial(I/A)/\partial X = \partial(\partial \bar{D}/\partial X)/\partial t = 0. \tag{59}$$

The voltage difference across the electrodes in Fig. 2 is

$$\Phi(t) = \int_0^{l_0} (\partial \hat{\phi}/\partial X) dX = -\int_0^{l_0} \bar{E} dX = RI. \tag{60}$$

Across the shock, the following jump conditions can be deduced from Eqs. (55) and (56):

$$T^+ - T^- = -\rho_0 V(v^+ - v^-), \quad \bar{D}^+ - \bar{D}^- = 0, \tag{61}$$

where + and − denote the values of a quantity immediately in front of and behind the shock. When the region in front of the shock (region 1) is unstressed and stationary, the first of Eq. (61) reduces to[23,24]

$$T = -\rho_0 V v, \tag{62}$$

where T and v are the normal stress and particle velocity in region 2. The second of Eq. (61) ensures that the surface charge density $\hat{\sigma}$ of Eq. (7) vanishes at the shock. Together the second of Eqs. (57) and (61) imply

$$\bar{D} = \bar{D}(t) \quad (0 \le X \le l_0). \tag{63}$$

The electric field is one dimensional; i.e., all components of $\hat{E}_A$ besides $\hat{E}_1 = \bar{E}$ vanish identically when $X_1 \to X$. Neither the stress state nor the polarization is necessarily one dimensional. Letting $X_1 \to X$, the axial components of thermodynamic tension and stress in region 2 become, from Eqs. (48) and (49),

$$\Sigma = C_{1111}E + (C_{111111}/2)E^2 + (\Upsilon_{CD}/2)\hat{P}_C\hat{P}_D + \Delta_{C11}\hat{P}_C - \beta_{11}\Delta\theta + J^{-2}\hat{P}_1(\Lambda_{1D}\hat{P}_D + \Delta_{111}E + \Upsilon_{1D}\hat{P}_D E), \tag{64}$$

$$T = J\Sigma + J^{-2}\bar{E}(\hat{P}_1 + \varepsilon_0\bar{E}/2). \tag{65}$$

When X_1 corresponds to a different system than that used to define material coefficients, then coefficients must be transformed to the laboratory frame. Care must be taken since piezoelectric coefficients can change sign upon reversal of loading direction. The temperature rise assuming adiabatic conditions is obtained from Eq. (26): $\Delta\theta = \theta_0[\exp(-\Gamma_{11}E) - 1]$, where Γ_{11} is Gruneisen's number in Eq. (39). In a physical experiment, particle velocity v is imposed; e.g., v is half the impact velocity if the striking material in a symmetric plate impact experiment is identical to that of the specimen.[23] Polarization, electric field, electric displacement, voltage difference, and current depend on the choice of electrical boundary conditions, in particular, the choice of resistance R in Fig. 2.

2. Voltage mode

Consider open circuit or voltage mode, where $R \to \infty$ and $I \to 0$ in Fig. 2 such that product RI remains finite. At $t=0$, assume polarization, electric field, and electric displacement vanish for $0 \le X \le l_0$. Then Eqs. (58) and (63) imply $\bar{D}=0$ throughout the specimen for the duration of the test. Relation (47) becomes

$$\bar{D} = 0 = \bar{\varepsilon}_1\bar{E}_1 = \bar{\varepsilon}_2\bar{E}_2 + \bar{P} \Leftrightarrow \bar{P} = -\bar{\varepsilon}_2\bar{E}_2, \tag{66}$$

where $\bar{P}$ is the X-component of strain-induced polarization $\bar{P}_A$ of Eq. (47) in region 2, $\bar{\varepsilon}_2(E)$ is the XX-component of the effective permittivity $\bar{\varepsilon}_{AB}$ in region 2, and $\bar{E}_2$ is the electric field in region 2, as illustrated in Fig. 2. Electric field and polarization remain zero in region 1, which exhibits constant permittivity $\bar{\varepsilon}_1$ throughout the experiment. No strain is induced in region 1. Strain, electric field, and polarization are constant in time but are generally nonzero within region 2. Assume that deformation gradient F is imposed in region 2 by to-be-determined magnitudes of particle velocity v and shock velocity V. Inverting Eq. (66) for the electric field in region 2, which will simply be labeled $\bar{E}$,

$$\bar{E} = \bar{E}_2 = -\bar{P}/\bar{\varepsilon}_2 = -(\bar{e}_2/\bar{\varepsilon}_2)E, \tag{67}$$

with $\bar{e}_2(E)$ the strain-dependent XXX-component of piezoelectric coefficient $\bar{e}_{ABC}$ of Eq. (47) in region 2. With the electric field in region 2 known from Eq. (67), the total polarization vector in region 2, from Eq. (45), is

$$\hat{P}_C = (\Lambda_{BC} + \Upsilon_{BC}E)^{-1}(JC_{B1}^{-1}\bar{E} - \Delta_{B11}E). \tag{68}$$

Expressions (67) and (68) can be substituted into Eqs. (48) and (49) to obtain all stress components, including normal stress T of Eq. (65). The particle velocity and shock velocity corresponding to compression $\gamma = 1 - F$ are

$$v = V\gamma, \quad V = \sqrt{-T/(\rho_0\gamma)}, \tag{69}$$

with $T<0$ for a compressive shock. In the linear elastic limit and in the absence of electromechanical effects, Eq. (69) reduces to $V \approx \sqrt{C_{1111}/\rho_0}$. The voltage difference across the electrodes is[43]

$$\Phi = -\int_0^{l_2} \bar{E}_2 dX - \int_{l_2}^{l_1+l_2} \bar{E}_1 dX = (\bar{e}_2/\bar{\varepsilon}_2) E l_2, \tag{70}$$

where instantaneous lengths of shocked and unshocked regions are

$$l_2 = (V-v)t, \quad l_1 = l_0 - Vt. \tag{71}$$

Wave transit time across the specimen is $t_0 = l_0/V$. The sign of $\bar{e}_2$ determines the signs of $\bar{P}$, $\bar{E}$, and Φ.

3. Current mode

Now consider short-circuit conditions, where $R \to 0$ in Fig. 2. At any instant of time, electric fields $\bar{E}_1$ and $\bar{E}_2$ are assumed spatially constant within respective regions 1 and 2 of the specimen. The electric potential difference is zero across the electrodes, so Eq. (60) becomes[23,24]

$$0 = \int_0^{l_2} \bar{E}_2 dX + \int_{l_2}^{l_1+l_2} \bar{E}_1 dX = \bar{E}_2 l_2 + \bar{E}_1 l_1. \tag{72}$$

Assuming for now that shock velocity V is constant, Eq. (71) applies. Clearly $\bar{E}_1$ and $\bar{E}_2$ are both time dependent. The compression of the piezoelectric specimen in shocked region 2 generates an electric field $\bar{E}_2$ in region 2, which in turn must be counteracted by an electric field $\bar{E}_1$ generated in region 1 ahead of the shock so that Eq. (72) is satisfied. Noting from Eq. (63) that electric displacement is identical in both regions,

$$\bar{D} = \bar{\varepsilon}_1 \bar{E}_1 = \bar{\varepsilon}_2 \bar{E}_2 + \bar{P}, \tag{73}$$

where $\bar{P}$ is the X-component of strain-induced polarization $\bar{P}_A$ in region 2 that depends on strain but is time independent within region 2,

$$\bar{P} = \bar{e}_2 E. \tag{74}$$

From Eqs. (72)–(74), the time-dependent electric field in the unshocked ($\bar{E}_1$) and shocked ($\bar{E}_2$) regions can be computed in terms of strain E in the shocked region as

$$\bar{E}_1 = [\bar{\varepsilon}_1 + (l_1/l_2)\bar{\varepsilon}_2]^{-1} \bar{e}_2 E, \quad \bar{E}_2 = -[\bar{\varepsilon}_2 + \bar{\varepsilon}_1 (l_2/l_1)]^{-1} \bar{e}_2 E. \tag{75}$$

With the electric field now known, the total polarization vector in region 2, from Eq. (45) is, with $\bar{E} = \bar{E}_2$,

$$\hat{P}_C = (\Lambda_{BC} + \Upsilon_{BC} E)^{-1} (J C_{B1}^{-1} \bar{E} - \Delta_{B11} E). \tag{76}$$

Relation (76) is then substituted into Eqs. (48) and (49) to obtain stress components, including T of Eq. (65). Particle velocity and shock velocity corresponding to compression $\gamma = 1 - F$ are obtained from Eqs. (52) and (62) as follows:

$$v = V\gamma, \quad V = \sqrt{-T/(\rho_0 \gamma)}, \tag{77}$$

noting that $T < 0$. Displacement current (58) for the open interval $0 < t < t_0$ is

$$\frac{I}{A} = \frac{d\bar{D}}{dt} \approx \frac{\bar{e}_2 (\bar{\varepsilon}_2/\bar{\varepsilon}_1)(1 - v/V)(\gamma^2/2 - \gamma)}{[(1 - v/V)(t/t_0) + (\bar{\varepsilon}_2/\bar{\varepsilon}_1)(1 - t/t_0)]^2}, \tag{78}$$

where Eq. (71) has been used, assuming V is constant.[23,24] Since the electric field is time dependent, axial stress T will not be strictly constant, implying that if a constant particle velocity is imposed, then strain γ and shock velocity V cannot both be constant for the duration of the experiment. Hence, the final expression in Eq. (78) is only approximate. A correction accounts for secondary strain generated in region 1 of the specimen as a result of induced electric field $\bar{E}_1$; Graham[23,24] labeled this effect "electromechanical coupling." This secondary strain affects the measured displacement current. The corrected current, derived by Stuetzer[64] and accounting for secondary strain in region 1, is

$$\frac{I}{A} = \frac{\bar{e}_2 (\bar{\varepsilon}_2/\bar{\varepsilon}_1)(1 - v/V)(\gamma^2/2 - \gamma)}{t_0 [(1 - v/V)(t/t_0) + (\bar{\varepsilon}_2/\bar{\varepsilon}_1)(1 - t/t_0)]^2} \exp(k^2 t/t_0), \tag{79}$$

where $t_0 = l_0/V$, acoustic impedances of electrodes are assumed to match, and for loading along $X = X_1$,

$$k^2 = (e_{111})^2/(\varepsilon_0 \varepsilon_{11} C_{1111}^{\hat{D}}). \tag{80}$$

At the instant immediately after impact ($t = 0^+$), $l_2 = 0$, $\bar{E}_1 = 0$, $\bar{E}_2 = -\bar{e}_2 E/\bar{\varepsilon}_2$, and

$$I/A = \bar{e}_2 (1 - v/V)(\gamma^2/2 - \gamma)/[t_0 (\bar{\varepsilon}_2/\bar{\varepsilon}_1)]. \tag{81}$$

Comparison with Eq. (67) indicates that electric field and stress in region 2 at $t = 0^+$ are the same as those under open-circuit conditions. At the instant the stress wave reaches the end of the specimen, $l_1 = 0$, $\bar{E}_2 = 0$, $\bar{E}_1 = \bar{e}_2 E/\bar{\varepsilon}_1$, and

$$I/A = \bar{e}_2 (\bar{\varepsilon}_2/\bar{\varepsilon}_1)(\gamma^2/2 - \gamma)\exp(k^2)/[t_0 (1 - v/V)]. \tag{82}$$

Dividing Eq. (82) by Eq. (81), the ratio of permittivity in strained and unstrained regions can be found by solving

$$I(t_0^-)/I(0^+) = [(\bar{\varepsilon}_2/\bar{\varepsilon}_1)/(1 - v/V)]^2 \exp(k^2). \tag{83}$$

In the application that follows, axial stresses T computed under conditions (81) and (82) are nearly identical. Hence, particle and shock velocities corresponding to a particular deformation (F, J, E, or γ) are constant in region 2 for the purposes of calculation.

B. Model predictions for 6H-SiC

It is assumed for the present calculations that deformation is elastic and homogeneous in the shocked region. The duration of loading is longer than t_0; i.e., release of the impacted edge of the specimen is not considered. Consideration of lattice defects, plastic yielding, and fracture is deferred to Sec. V. It is also assumed that α-SiC behaves as a dielectric with no free charges. Presumably, above some threshold impact velocity, this assumption may be inappropriate. The electric field generated in region 2 of the disk as a result of the piezoelectric effect may be strong enough to induce dielectric breakdown, as has been observed in quartz,[65,66] which has a higher band gap and higher breakdown field under ambient conditions:[67] ~9 eV and 13–15 MV/cm for

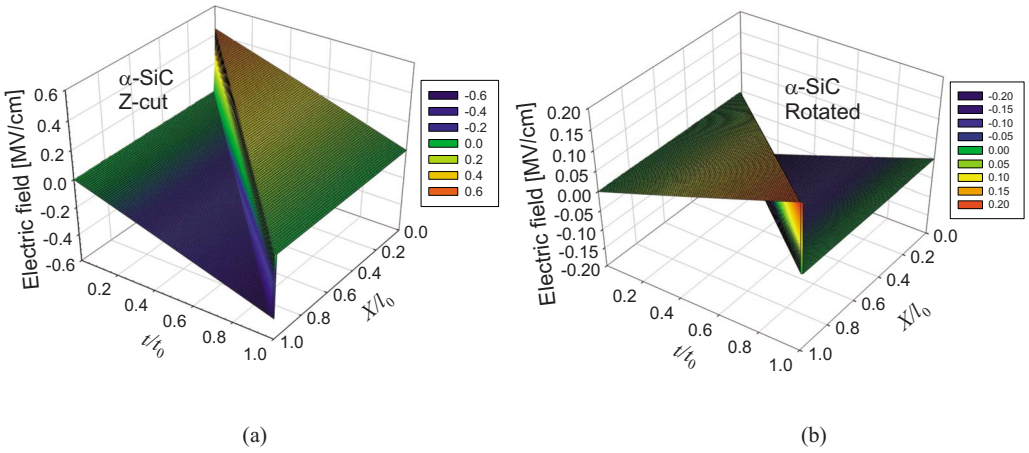

FIG. 3. (Color online) Predicted material electric field in α-SiC at 1% compression (γ=0.01): (a) Z-cut and (b) rotated cut.

SiO_2 versus ~3 eV and 2–4 MV/cm for 6*H*-SiC. When breakdown occurs, free electrons can contribute to the current, and the second of Eq. (57) does not apply.

Considered is a disk of thickness l_0=6.35 mm, the same dimension as quartz specimens considered by Graham *et al.*[68] Computed are responses for four different single crystal orientations, loaded in axial compression over the range $0 < \gamma \leq 0.1$ (i.e., $1 > J \geq 0.9$), under both voltage and current modes. For the Z-cut orientation, the shock wave is directed along the X_3-axis of Fig. 1, i.e., in the positive [0001] direction. In the −Z-cut orientation, the shock wave travels along the $-X_3$-axis of Fig. 1. A different electrical response results for these two orientations (±Z-cut) because the sign of piezoelectric constant e_{33} is reversed upon rotation of the crystal by 180° about an axis in the basal plane. In the X-cut orientation, the wave travels in the X_1-direction of Fig. 1, i.e., in the positive $[\bar{1}2\bar{1}0]$ direction. The rotated cut crystal is equivalent to the Z-cut crystal rotated counterclockwise about the X_1-axis by an angle of 54.03°, with the shock then propagating in the positive direction along the laboratory X_3-axis. The assumption that a wave remains planar in an anisotropic crystal is most valid when the crystal is loaded along certain directions.[69] For each orientation considered here, an elastic wave propagates in such a "pure mode" direction dictated by second-order elastic constants of 6*H*-SiC.

Predicted material electric fields $\bar{E}_1$ and $\bar{E}_2$ of Eq. (72) are shown in Fig. 3 for short-circuit (current mode) loading with an impact velocity producing a compressive strain of γ=0.01. The results in Fig. 3 can be interpreted by considering Eq. (72). The shock (stress) wave front is the surface of discontinuity along the diagonal $X/l_0 = t/t_0$. As the stress wave propagates through the specimen, the magnitude of the electric field behind the front decreases in conjunction with an increase in length l_2 of the stressed region. Simultaneously, the electric field ahead of the front increases in magnitude in conjunction with a decrease in length l_1. The algebraic sign of the electric field in each region is dictated by the sign of piezoelectric coefficient $\bar{e}_2$, which in turn depends on the orientation of the crystal. Maugin[43] presented theoretical results for shock-loaded ferroelectric crystals of PZT 65/35 in a similar graphical format. The electric field for the Z-cut specimen is shown in Fig. 3(a); the field for the −Z-cut specimen, not shown, is equal in magnitude but opposite in sign to that shown in Fig. 3(a). The electric field for the rotated-cut specimen in Fig. 3(b) is similar to that of the −Z-cut specimen, but smaller in magnitude by about a factor of 3. In all cases, the maximum magnitude of the electric field in the shocked region arises at the instant after impact ($t=0^+$), and the maximum in the unshocked region arises at $t=t_0^-$. No electric field is generated in an impact experiment on an X-cut specimen because e_{11}=0. The spatial electric field $\hat{e}$ of Eq. (54) in the shocked region for voltage mode loading is shown in Fig. 4 over a range of compressive strains; recall from Eq. (81) that this is the same field that would be generated at $t=0^+$ under current mode loading. The regime where dielectric breakdown would occur under ambient pressure is indicated;[67] however, the electric field required for dielectric breakdown may depend on pressure, as has been observed in quartz.[65] The predictions in Figs. 3 and 4 are valid so long as the material response remains elastic; however, yield via slip or fracture could occur prior to attainment of strains on the order of 0.1, as discussed in Sec. V.

Normal stresses of Eq. (65) are shown in Fig. 5(a). The predictions shown for single crystals presume an adiabatic elastic response under voltage mode conditions (equivalent to the stress under current mode at $t=0^+$). The effects of anisotropy are clear, with normal stress highest for Z-cut and lowest for rotated-cut specimens. Single crystal stresses may be overestimated in Fig. 5(a) if yielding occurs and the shear

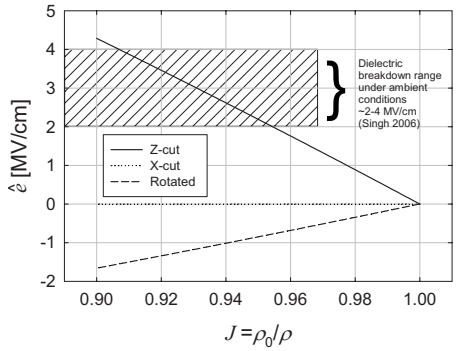

FIG. 4. Predicted spatial electric field behind shock front in α-SiC under voltage mode loading. Field for −Z-cut specimen (not shown) is equal in magnitude and opposite in sign to that of Z-cut specimen.

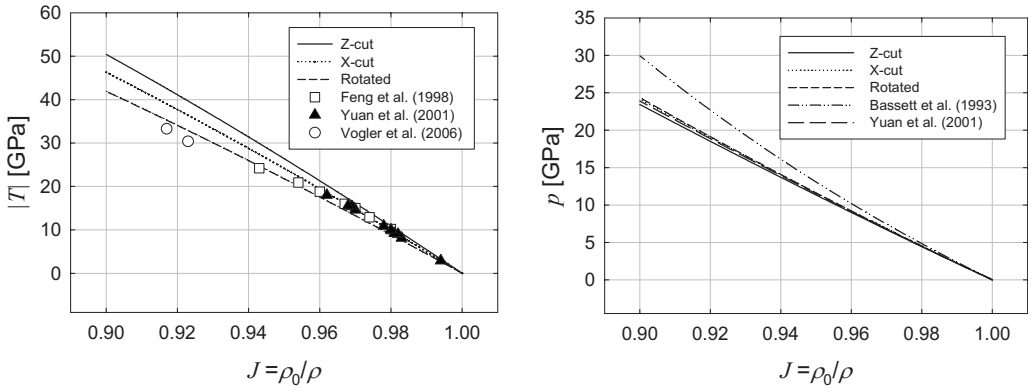

(a) (b)

FIG. 5. Normal stress (a) and Cauchy pressure (b) in α-SiC under voltage mode loading. Stress and pressure for $-$Z-cut specimen (not shown) are identical to those of Z-cut. The marked points in (a) correspond to experiments on polycrystalline SiC–B from Refs. 13, 37, and 70. The curves in (b) from Refs. 59 and 70 correspond to the results obtained from the experiments on polycrystalline α-SiC.

strength decreases relative to that of an elastic crystal. The data from impact experiments on polycrystalline α-SiC are shown for comparison; for $J<0.96$, yielding occurred in the experiments.[13,37,70] Hydrostatic pressure $p=-\sigma_{aa}/3$ is shown in Fig. 5(b) under the same loading conditions. Predicted pressure varies little with crystal orientation under uniaxial compressive loading, and is similar to the results of Yuan *et al.*,[70] the latter following from the analysis of *in situ* measurements, with electromagnetic velocity gauges, for impact-loaded polycrystalline SiC–B.

While model predictions of pressure seem to agree most closely with those of Yuan *et al.*,[70] such predictions should not be interpreted as an affirmation of greater accuracy of one set of published experimental results over another. Yuan *et al.*[70] found that their analysis and data fit [their Eq. (10), reproduced here in Fig. 5(b)] closely agree to pressures up to $\sim$15 GPa, with experimental results of Feng *et al.*[37] obtained using lateral manganin foil gauges on different specimens of the same material loaded in plate impact (see Fig. 9 of Yuan *et al.*[70]). The response of Bassett *et al.*,[59] obtained from static compression using a diamond anvil cell and x-ray diffraction (to 68.4 GPa), agrees closely with the experimental results of Amulele *et al.*[71] obtained using ultrasonic measurements (to 13.6 GPa) and x-ray measurements in a diamond anvil cell (to 27 GPa). The upper curve shown in Fig. 5(b), i.e., that used explicitly by Bassett *et al.*,[59] corresponds to a Birch–Murnaghan equation of state (EOS) with bulk modulus of 230.2 GPa and pressure derivative of bulk modulus of 4. The curve of Yuan *et al.*[70] was fitted by those authors to impact data at up to $\sim$4% volumetric compression; hence this curve represents an extrapolation to higher pressures in Fig. 5(b). The curve corresponding to Bassett *et al.*[59] does not represent an extrapolation. Bassett *et al.*[59] noted that their static measurements indicated a stiffer response than the shock measurements of Kipp and Grady.[72] Differences in experimental techniques (e.g., static versus dynamic) and sample variations (e.g., second phases, defects, and porosity) could account for differences among experimental results. A more extensive survey of compression studies on polycrystalline SiC is given by Dandekar.[9]

Predictions for single crystals in Fig. 5 are calculated using the finite strain anisotropic elasticity theory of Sec. III B, with material properties obtained from independent sources (Tables I and II). In particular, if third-order elastic constants entering the model are not accurate, or if fourth-order elastic constants are important (e.g., as may be the case

TABLE III. Predicted shock response: Z-cut ([0001]) orientation.

Axial compression			Axial stress magnitude, $\|T\|$ (GPa)					
γ	J	Particle velocity, v (km/s)	Open circuit	Short circuit ($t=t_0^-$)	Breakdown ($\hat{P}_A=0$)	Isothermal ($\beta_{AB}=0$)	$\frac{\partial C_{AB}}{\partial p}=0$	$Y_{AB}=0$
0.01	0.99	0.1303	5.4537	5.4362	5.4556	5.4474	5.4124	5.4537
0.02	0.98	0.2597	10.8238	10.7896	10.8274	10.8113	10.6618	10.8238
0.03	0.97	0.3880	16.1071	16.0567	16.1122	16.0884	15.7498	16.1070
0.04	0.96	0.5152	21.3003	21.2346	21.3068	21.2757	20.6781	21.3003
0.05	0.95	0.6413	26.4006	26.3202	26.4083	26.3702	25.4483	26.4006
0.06	0.94	0.7662	31.4051	31.3106	31.4138	31.3690	30.0621	31.4051
0.07	0.93	0.8898	36.3111	36.2030	36.3206	36.2694	34.5211	36.3110
0.08	0.92	1.0123	41.1158	40.9949	41.1260	41.0688	38.8270	41.1158
0.09	0.91	1.1334	45.8169	45.6836	45.8277	45.7645	42.9813	45.8168
0.10	0.90	1.2532	50.4119	50.2667	50.4230	50.3544	46.9858	50.4118

TABLE IV. Predicted shock response: X-cut ($[\bar{1}2\bar{1}0]$) orientation.

Axial compression			Axial stress magnitude, $\|T\|$ (GPa)					
γ	J	Particle velocity, v (km/s)	Open circuit	Short circuit ($t=t_0^-$)	Breakdown ($\hat{P}_A=0$)	Isothermal ($\beta_{AB}=0$)	$\frac{\partial C_{AB}}{\partial p}=0$	$Y_{AB}=0$
0.01	0.99	0.1245	4.9788	4.9788	4.9837	4.9716	4.9374	4.9787
0.02	0.98	0.2482	9.8882	9.8882	9.8977	9.8739	9.7262	9.8880
0.03	0.97	0.3710	14.7249	14.7249	14.7389	14.7037	14.3677	14.7246
0.04	0.96	0.4928	19.4857	19.4857	19.5039	19.4577	18.8634	19.4850
0.05	0.95	0.6135	24.1673	24.1673	24.1895	24.1327	23.2150	24.1664
0.06	0.94	0.7333	28.7668	28.7668	28.7928	28.7257	27.4238	28.7655
0.07	0.93	0.8519	33.2814	33.2814	33.3110	33.2339	31.4914	33.2796
0.08	0.92	0.9694	37.7081	37.7081	37.7412	37.6544	35.4193	37.7058
0.09	0.91	1.0857	42.0444	42.0444	42.0807	41.9847	39.2088	42.0416
0.10	0.90	1.2008	46.2878	46.2878	46.3271	46.2222	42.8617	46.2844

in shocked quartz[23]), the finite strain elasticity model could underpredict axial stress and pressure at large compressive strains. It is also noted that single crystal predictions do not reflect porosity, grain boundaries, and other defects present in polycrystalline samples. Future impact experiments on single crystals of 6*H*-SiC could provide a check of the modeling results, could enable evaluation of accuracy and applicability of third-order elastic constants used here (from atomic modeling[27]), and could suggest whether inclusion of fourth-order elastic constants, whose values are presently unknown for α-SiC single crystals, would improve the predictions of the present model.

Tables III–V list the predicted axial stresses versus compressive strain for specimens of Z-cut, X-cut, and rotated-cut orientations, respectively, in strain increments of 1%. Stresses for the $-$Z-cut orientation are identical to those for Z-cut orientation in Table III. Particle velocities required to achieve tabulated compressions under open-circuit mode are listed. Listed in column 5 of each table is axial stress for current mode loading at the instant stress wave transit through the disk is complete. The stresses in column 6 correspond to dielectric breakdown under voltage mode, in which case shocked SiC is idealized as a conductor: null polarization, null electric field, and null electric displacement for open-circuit loading. The results in column 6 are what would be obtained if all piezoelectric and electrostriction coefficients were set identically to zero. Column 7 corresponds to an isothermal, as opposed to adiabatic, event, or equivalently to stress observed under null thermal expansion. The results in column 8 correspond to null third-order elastic constants, i.e., linear elasticity. The results in column 9 correspond to null electrostriction. From the results in Tables III–V, electromechanical effects and thermal effects provide a negligible influence on the axial stress for compressive strains up to $\gamma=0.1$. For example, from Table III, the stress difference between open- and short-circuit conditions is at most 0.4%, justifying the assumption of constant shock velocity used in calculations for current mode loading. Adiabatic temperature rises for $\gamma\leq 0.1$ were $\Delta\theta<33$ K, leading to the very small differences between stresses in columns 4 and 7. Omission of piezoelectricity and electrostriction (columns 5 and 7) likewise has an insignificant effect on the stress. The axial components of Maxwell's stress in Eq. (13) were three or four orders of magnitude smaller than the total stress T in Z-cut and rotated-cut orientations, and vanish entirely for X-cut specimens. Nonlinear elastic properties, on the other hand, do appear to be of importance in stress predictions for compressive strains of magnitudes considered

TABLE V. Predicted shock response: rotated orientation.

Axial compression			Axial stress magnitude, $\|T\|$ (GPa)					
γ	J	Particle velocity, v (km/s)	Open circuit	Short circuit ($t=t_0^-$)	Breakdown ($\hat{P}_A=0$)	Isothermal ($\beta_{AB}=0$)	$\frac{\partial C_{AB}}{\partial p}=0$	$Y_{AB}=0$
0.01	0.99	0.1180	4.4722	4.4697	4.4742	4.4653	4.4309	4.4722
0.02	0.98	0.2354	8.8903	8.8854	8.8942	8.8766	8.7283	8.8903
0.03	0.97	0.3519	13.2507	13.2435	13.2564	13.2304	12.8936	13.2506
0.04	0.96	0.4676	17.5501	17.5406	17.5574	17.5233	16.9281	17.5499
0.05	0.95	0.5825	21.7851	21.7735	21.7940	21.7519	20.8332	21.7847
0.06	0.94	0.6965	25.9526	25.9389	25.9630	25.9132	24.6101	25.9521
0.07	0.93	0.8095	30.0495	30.0339	30.0614	30.0041	28.2603	30.0489
0.08	0.92	0.9215	34.0730	34.0555	34.0861	34.0216	31.7851	34.0721
0.09	0.91	1.0325	38.0201	38.0009	38.0346	37.9630	35.1857	38.0191
0.10	0.90	1.1423	41.8884	41.8674	41.9039	41.8256	38.4637	41.8872

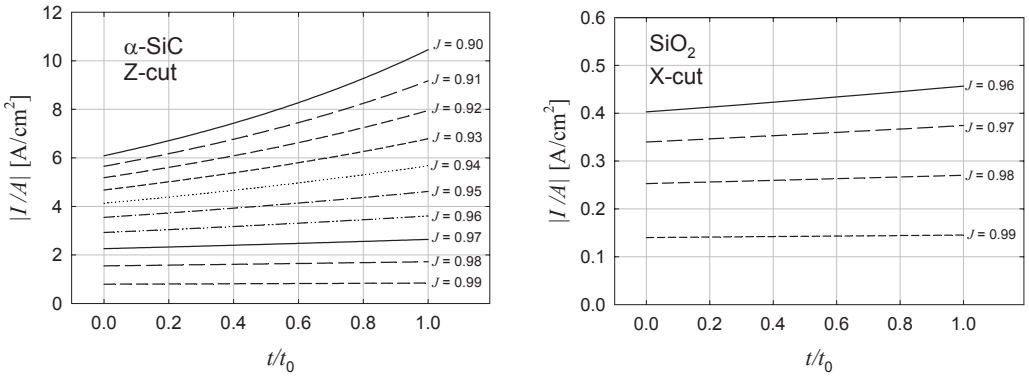

(a) (b)

FIG. 6. Displacement currents: (a) model prediction in shock-loaded Z-cut α-SiC and (b) reproduced using Eq. (79) and strain-dependent dielectric and piezoelectric coefficients obtained from impact experiments (Ref. 23) on X-cut quartz.

here. For example, for the Z-cut orientation, the stress of column 4 is underpredicted by linear elasticity in column 8 by 2% at a strain of 0.03 and by 7% at a strain of 0.1.

Conclusions regarding the importance of material parameters follow from the assumption that parameters are precisely known. Experimental uncertainty in elastic and piezoelectric constants will lead to uncertainty in model predictions that may overwhelm differences among the results in columns in Tables III–V. It follows that unless relevant material parameters in Tables I and II are known with sufficient precision, electromechanical and thermal effects can be omitted in stress predictions of uniaxial compression of 6*H*-SiC so long as the material remains elastic and strains remain in the range considered here. Nonlinear elasticity appears important however, as has been noted for other hexagonal or trigonal ceramics deformed similarly.[21–24] If fourth-order elastic constants are significant, as has been observed for quartz,[23] differences between linear and nonlinear elastic model predictions could be even greater.

The displacement current predicted in Z-cut quartz under current mode loading is shown in Fig. 6. The predictions for the range $1>J\geq 0.9$ are shown for illustrative purposes, though dielectric breakdown and/or plastic slip may occur prior to attainment of the larger compressive strains, e.g., for $J<0.96$, with the possibility of breakdown evident in Fig. 4. Analogous results for X-cut quartz are shown in Fig. 6(b) for a specimen of the same thickness. Current profiles in Fig. 6(b) were generated by substituting, into Eq. (79), the strain-dependent dielectric and piezoelectric coefficients and the shock velocity versus particle velocity relationship obtained from impact experiments on quartz by Graham.[23] [Graham[23] did not publish raw current versus time data for multiple experiments, so reproduction of the curves shown in Fig. 6(b) using Eq. (79) was necessary to enable comparison with Fig. 6(a).] The magnitude of the current predicted for SiC is significantly greater than that for SiO_2 because of the larger piezoelectric constant and larger wave speed in the former. The range of compressions in Fig. 6(b) is limited to $J\geq 0.96$ since inelasticity and dielectric breakdown ensued in quartz at larger compression.[23] Graham and Ingram[66] suggested that dislocations affect the conductivity of shock-loaded quartz; hence correlation between breakdown and the HEL is plausible.

V. PLASTICITY AND LATTICE DEFECTS

The model of Secs. II and III is extended to address plasticity and defects in dielectrics. The mechanisms pertinent to α-SiC are emphasized; comparisons with experiment are made to the extent permitted.

A. Kinematics

For crystalline solids with lattice defects, deformation gradient (1) is decomposed as[22,47]

$$F_{aA}=\partial_A x_a=F^E_{a\alpha}(\bar{J}^{1/3}\delta_{\alpha\beta})F^P_{\beta A}, \tag{84}$$

where Greek subscripts represent tensor indices referred to a Cartesian coordinate system in the elastically unloaded intermediate configuration of the body. The thermoelastic deformation is $F^E_{a\alpha}$, the isochoric plastic deformation associated with dislocation glide is $F^P_{\beta A}$, and scalar $\bar{J}$ accounts for volume changes from point defects[73,74] as well as residual elastic volume changes associated with residual stress fields of dislocations.[22,47,74–77] When $\bar{J}=1$, Eq. (84) reduces to the usual kinematics of finite plasticity theory.[46,78] The plastic velocity gradient referred to the intermediate configuration is[22,46]

$$L^P_{\alpha\beta}=\dot{F}^P_{\alpha A}F^{P-1}_{A\beta}=\sum_i \dot{\gamma}^i \bar{s}^i_\alpha \bar{m}^i_\beta, \tag{85}$$

where $\dot{\gamma}^j$, $\bar{s}^i_\alpha$, and $\bar{m}^i_\beta$ are the slip rate, unit slip direction, and unit slip plane normal for slip system i. The slip system geometry is mapped to the current configuration via $s^i_a=F^E_{a\alpha}\bar{s}^i_\alpha$ and $m^i_a=\bar{m}^i_\alpha F^{E-1}_{\alpha a}$. Since $\bar{s}^i_\alpha \bar{m}^i_\alpha=0$, $L^P_{\alpha\alpha}=0$ and plastic deformation is isochoric. The total volume change is

$$J=\det(F_{aA})=\det(F^E_{a\alpha})\bar{J}=J^E\bar{J}. \tag{86}$$

Mass density in the intermediate configuration is $\bar{\rho}=\rho J^E=\rho_0\bar{J}^{-1}$. Relations (1)–(18) still apply.

TABLE VI. Slip systems, Burgers vectors, and slip plane spacing.

Type	Direction	Plane	Burgers **b**	b (nm)	d (nm)
Basal, full	$\langle 1\bar{2}10\rangle$	(0001)	$1/3[1\bar{2}10]$	0.308	0.252
Basal, partial	$\langle 1\bar{1}00\rangle$	(0001)	$1/3[1\bar{1}00]$	0.178	0.252
Prism, full	$\langle 1\bar{2}10\rangle$	$\{10\bar{1}0\}$	$1/3[1\bar{2}10]$	0.308	0.267

B. Thermodynamics

For an elastic-plastic dielectric with lattice defects, free energy (19) is replaced with

$$\psi = \psi(E^E_{\alpha\beta}, \bar{p}_\alpha, \theta, \xi^k), \tag{87}$$

where finite elastic deformation and strain tensors are, respectively,

$$C^E_{\alpha\beta} = F^E_{a\alpha}F^E_{a\beta}, \quad E^E_{\alpha\beta} = (C^E_{\alpha\beta} - \delta_{\alpha\beta})/2. \tag{88}$$

Polarization, electric field, and electric displacement mapped to the intermediate configuration are[45]

$$\bar{p}_\alpha = F^E_{a\alpha}\hat{p}_a, \quad \bar{e}_\alpha = F^E_{a\alpha}\hat{e}_a, \quad \bar{d}_\alpha = J^E F^{E-1}_{\alpha a}\hat{d}_a. \tag{89}$$

Symbol ξ^k $(k=1,2,\ldots,n)$ represents scalar defect densities for n kinds of defects. For example, in Sec. V D, ξ^k is used to represent dislocations and vacancies in α-SiC. The dependence of free energy on ξ^k accounts for self- and interaction energies of defects contained within a representative volume element of defective crystal. Stress power in Eqs. (16) and (18) can be expressed per intermediate volume as

$$J^E\sigma_{ab}L_{ab} = \bar{P}_{a\alpha}\dot{F}^E_{a\alpha} + \sum_i \bar{\tau}^i\dot{\gamma}^i + \bar{\sigma}\dot{J}J^{-1}, \tag{90}$$

with $\bar{P}_{a\alpha} = J^E\sigma_{ab}F^{E-1}_{\alpha b}$, $\bar{\tau}^i = J^E\sigma_{ab}s^i_a m^i_b$ a resolved shear stress on slip system i, and $\bar{\sigma} = -J^E p$ with p the Cauchy pressure. Thermodynamic admissibility is ensured when Eq. (20) applies and when the following constitutive relationships apply in lieu of Eqs. (21) and (22):

$$\bar{\Sigma}_{\alpha\beta} = J^E F^{E-1}_{\alpha a}\sigma_{ab}F^{E-1}_{\beta b} = F^{E-1}_{\alpha a}\bar{P}_{a\beta} = \bar{\rho}\frac{\partial\psi}{\partial E^E_{\alpha\beta}} + J^E C^{E-1}_{\alpha\chi}\bar{p}_\chi C^{E-1}_{\beta\delta}\bar{e}_\delta, \tag{91}$$

$$\hat{e}_a = F^E_{a\alpha}\rho\frac{\partial\psi}{\partial\bar{p}_\alpha}, \quad \bar{e}_\alpha = J^{E-1}C^E_{\alpha\beta}\bar{\rho}\frac{\partial\psi}{\partial\bar{p}_\beta}. \tag{92}$$

Multiplying Eq. (18) by J^E, the dissipation inequality becomes

$$\sum_i \bar{\tau}^i\dot{\gamma}^i + \bar{\sigma}\dot{J}J^{-1} - \bar{\rho}\sum_k \frac{\partial\psi}{\partial\xi^k}\dot{\xi}^k + J^E\theta^{-1}q^a\partial_a\theta \geq 0. \tag{93}$$

The first term in Eq. (93) accounts for dissipation from dislocation glide, the second accounts for dissipation from inelastic volume changes, the third for stored energy of defects, and the fourth for heat conduction.

To this point, Sec. V has been general in scope. Specifically for defective α-SiC, Eq. (27) is replaced with

$$\begin{aligned}\rho_0\psi = {} & (1/2)C_{\alpha\beta\chi\delta}E^E_{\alpha\beta}E^E_{\chi\delta} + (1/6)C_{\alpha\beta\chi\delta\varepsilon\phi}E^E_{\alpha\beta}E^E_{\chi\delta}E^E_{\varepsilon\phi} \\ & + (1/2)\Lambda_{\alpha\beta}\bar{p}_\alpha\bar{p}_\beta + \Delta_{\alpha\beta\chi}\bar{p}_\alpha E^E_{\beta\chi} \\ & + (1/2)\Upsilon_{\alpha\beta\chi\delta}\bar{p}_\alpha\bar{p}_\beta E^E_{\chi\delta} - \beta_{\alpha\beta}E^E_{\alpha\beta}\Delta\theta - \rho_0 c\,\theta\ln(\theta/\theta_0) \\ & + W(\xi^k).\end{aligned} \tag{94}$$

Defect energy per unit reference volume is W. Material coefficients with Greek indices in Eq. (94) are defined by replacing E_{AB} with $E^E_{\alpha\beta}$ and $\hat{P}_A$ with $\bar{p}_\alpha$ in Eqs. (28), (32), and (35). These coefficients have the same numerical values as those obtained from Tables I and II. In the absence of defects and inelasticity, $W=0$, $F_{aA}=F^E_{a\alpha}\delta_{\alpha A}$, and Eq. (94) becomes identical to Eq. (27).

C. Inelastic shear: Plastic slip and fracture

Rate equations for dislocation glide in semiconductor crystals such as SiC can be written as[17]

$$\dot{\gamma}^i = A\left|\frac{\bar{\tau}^i}{\tau_C}\right|^{1/m}\frac{\bar{\tau}^i}{|\bar{\tau}^i|}\exp\left(\frac{-Q}{k_B\theta}\right), \tag{95}$$

where A is a positive constant, $\tau_C > 0$ is the slip resistance that may vary among different families of slip systems, $m = \partial \ln \bar{\tau}^i / \partial \ln \dot{\gamma}^i$ is a rate sensitivity, Q is an activation energy, and k_B is the Boltzmann's constant. Superscript i corresponds to a particular slip system with resolved shear stress $\bar{\tau}^i$. Other functional forms of kinetic equations are possible.[16,42,79] In α-SiC, Q may depend on electric current to account for lowering of the energy barrier to dislocation migration under bias voltage.[5,14]

Table VI describes the slip systems and Burgers vectors in α-SiC. Relevant dislocations in hexagonal polytypes are partial mixed dislocations on basal planes formed from the dissociation[5,14,16,17,80]

$$\tfrac{1}{3}[1\bar{2}10] \rightarrow \tfrac{1}{3}[1\bar{1}00] + \tfrac{1}{3}[0\bar{1}10]. \tag{96}$$

Full dislocations on the left of Eq. (96) have $b=$a and tangent lines oriented at 60° from $[1\bar{2}10]$, while Shockley partials on the right have $b=\text{a}/\sqrt{3}$ and tangent lines oriented at 30° and 90° from their respective Burgers vector directions (i.e., a mixed partial and a pure edge partial). At ambient temperatures, because of the high Peierls potential in SiC, partials are predominantly straight.[80] Core structures of Shockley partials on the basal plane may terminate at C or Si atoms;[5] the termination type affects the properties of the dislocation, including core energy and mobility. Full $1/3\langle 1\bar{2}10\rangle$ dislocations on $\{10\bar{1}0\}$ prism planes in loop configurations have been found in specimens subject to indentation at room temperature and could have comparable mobility to straight

TABLE VII. Measured or predicted properties for slip or yield.

Parameter	Value	Dislocation type	Definition	Ref.
τ	5.7 ± 1.3 GPa	Unknown	Shear strength; shocked polycrystal	37
	2.4 ± 1.0 GPa	Unknown	Shear strength; shocked polycrystal	13
	6.8 GPa	Unknown	Shear strength; static compression	4
	4.5 ± 0.4 GPa	Unknown	Shear strength; indentation	38
τ_C	1.24 GPa	Basal 60°	Peierls–Nabarro stress	Equation (97)
	0.70 GPa	Prism edge	Peierls–Nabarro stress	Equation (97)
m	3.0 ± 0.7	Partial basal	Rate sensitivity of yield stress	16
Q	2.5 eV	Partial basal	Activation energy; null bias	16
	0.27 eV	Partial basal	Activation energy; $\lvert I/A \rvert = 0.5$ A/cm^2	14

basal plane partials;[80] however, much less seems known about the core structure and energetic properties of these prismatic dislocations. Merala *et al.*[2] noted that secondary slip on prism planes may occur in shock-loaded hexagonal SiC, and this mechanism was considered in the simulations of Zhang *et al.*[40] At temperatures below 1400 K, partial dislocations are favored over full dislocations, with leading partials more mobile than trailing partials in 4*H*- and 6*H*-SiC.[16,17,80] The trailing partial may not nucleate at all; hence large numbers of stacking faults are often generated during slip. Stacking fault energy[80] associated with Shockley partials in Eq. (96) is $W_{SF} \approx 2.5$ mJ/m^2, one to two orders of magnitude smaller than that typical for metals,[81] explaining the tendency for Eq. (96) to occur. Above 1400 K, plasticity in α-SiC tends to manifest by collective motion of leading and trailing partials rather than by leading partials alone.[16,17,80]

Measurements of shear strength of 6*H*-SiC are listed in Table VII. Values for shocked polycrystals correspond to impact stresses at or above the HEL, where for an isotropic response, $\tau = 3(|T| - p)/4$. Also listed are shear stresses required to enact motion of full basal and prism dislocations via the Peierls–Nabarro model,[82,83] where the critical shear strength is

$$\tau_C = 2\hat{K} \exp[-2\pi\hat{K}d/(\mu b)], \tag{97}$$

with $\hat{K}$ the energy factor accounting for anisotropic elasticity[5,83] and d the distance between slip planes. In the isotropic approximation, $\hat{K} = \mu$ for a screw dislocation and $\hat{K} = \mu/(1-\nu)$ for an edge dislocation. The Peierls model has been posited as a reasonable estimate for slip resistance in other ceramics.[22,84] Two other estimates, not listed in Table VII, have been suggested. For slip of partial basal dislocations, Maeda *et al.*[80] suggested a shear strength of $W_{SF}/b \approx 0.014$ GPa. Zhang *et al.*[40] proposed shear strengths of 4.3 GPa for full basal dislocations and 7.5 GPa for full prism dislocations upon comparison of continuum simulations with data for polycrystalline normal and shear stresses from shock physics experiments.

Strain rate sensitivity and activation energy for slip of leading partial dislocations are also listed in Table VII. Activation energy Q drops by an order of magnitude in the presence of a current of magnitude 0.5 A/cm^2. Blumenau *et al.*[5] found an activation energy of 2.1–4.8 eV for slip in 2*H*-SiC at null bias, with the particular value of Q depending on dislocation orientation and location of the core at either Si–Si or C–C bonds. The mobility of C-terminated partials was found to be higher than that of Si-terminated partials in 2*H*-SiC. The recombination enhanced dislocation glide (REDG) mechanism, whereby electronic structures of dislocation cores and stacking faults change as a result of current injection under forward bias voltage, is thought to influence the mobility of partial dislocations and hence explain the reduction in activation energy with current or bias voltage in cubic and hexagonal polytypes of SiC.[5,14,15] As is clear from Table VIII, at strain $\gamma = 0.024$ corresponding to the HEL in polycrystals,[37] the magnitude of the current—as predicted by model solutions of Sec. IV—in Z-cut and rotated-cut specimens exceeds that needed to induce the reduction in activation energy for glide of basal partials, at electric field strengths lower than those that would induce dielectric breakdown.[67] Thus, it is conceivable that different slip resistances could be observed in single crystals of 6*H*-SiC loaded in current mode (e.g., reduced Q due to REDG mechanism) and voltage mode (e.g., no current and no reduction in Q). Experiments are needed, however, to determine if the REDG mechanism occurs as a result of displacement currents generated at high pressures, and what effect electric field may have on dislocation mobility in SiC at high pressures.

Fracture properties are listed in Table IX. A fundamental quantity considered in failure models for single crystals deformed at high pressure is the theoretical shear strength[21,22,85]

TABLE VIII. Predicted current and electric field in 6*H*-SiC at polycrystalline HEL ($\gamma = 0.024$).

Orientation	Current, $\lvert I/A \rvert$ (A/cm^2) $t = 0^+$	Current, $\lvert I/A \rvert$ (A/cm^2) $t = t_0^-$	Electric field, $\lvert \hat{e} \rvert$ (MV/cm)
Z-cut	1.840	2.086	1.039
Rotated cut	0.624	0.705	0.403

TABLE IX. Fracture properties.

Plane	Theoretical strength, τ_C (GPa)[a]	Cohesive energy (J/m^2) [b]
(0001)	37.7	8.6 ± 0.4
$\{10\bar{1}0\}$	35.6	5.6 ± 0.5
$\{\bar{1}2\bar{1}0\}$	61.8	4.0 ± 0.2

[a]Reference 83.
[b]Reference 20.

$$\tau_C = \mu b/(2\pi d), \tag{98}$$

with d the spacing between cleavage planes and b the magnitude of Burgers vector of a full dislocation on such planes. Cohesive energies listed were obtained from indentation.[20]

Examination of shear stresses predicted in nonlinear elastic calculations provides insight into possible inelastic mechanisms that may arise in shock-loaded crystals of α-SiC. Figure 7 shows the maximum shear stress $\tau=(T_{\max}-T_{\min})/2$ computed for single crystals of Z-cut, X-cut, and rotated orientations, where $T_{\max}$ and $T_{\min}$ are the maximum and minimum principal values of stress tensor (49). The effects of anisotropy are evident from differences in shear stress among different orientations. The data from experiments[13,37] on SiC–B are shown for comparison. Clearly nonlinear elasticity calculations for the single crystal response do not account for the loss of some, but not all, shear strength above the HEL observed in polycrystals.[13,37] Polycrystals could fail by grain boundary mechanisms not considered in the single crystal calculations.

Figure 8 shows, versus uniaxial deformation, resolved shear stress $\bar{\tau}=\max \bar{\tau}^i$ among all prism or basal systems (Table VI), normalized by the Peierls stress for prism or basal slip listed in Table VII. Also shown are maximum resolved shear stresses on prism and basal planes, normalized by the theoretical shear strengths of Table IX. Only the results for X-cut [Fig. 8(a)] and rotated cut [Fig. 8(b)] crystals are shown. For $\pm$Z-cut specimens loaded in uniaxial strain, no such slip or fracture mechanisms are active since no shear stresses act on basal or any prism planes. For X-cut specimens, basal slip and basal plane fracture cannot occur since no shear stresses act on the basal plane. For the X-cut orientation, prism slip appears likely, and fracture on prism planes

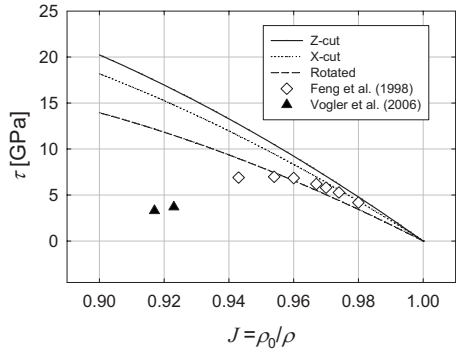

FIG. 7. Predicted maximum shear stress in α-SiC under voltage mode loading. The data points from Refs. 13 and 37 correspond to impact experiments on polycrystalline SiC–B.

unlikely, since the Peierls stress is exceeded for $J<0.995$ but the theoretical stress is never approached, even at $J=0.1$. For the rotated orientation, both prism and basal slip are possible at strains less than the polycrystalline HEL if the Peierls prediction of shear strength is reasonable. The theoretical strength is not approached on prism or basal planes in the rotated orientation, even at $J=0.1$. In real crystals, however, fracture could be induced by stress concentrations at preexisting or nucleated defects such as (piled-up) sessile dislocations.[79,81]

D. Defect energies and volumes

Defect energy W in Eq. (94) is written as a sum of contributions from dislocations, point defects, and stacking faults

$$W = \sum_l [(W_E + W_C)\rho_D] + \sum_p [W_F \varsigma_V] + \sum_r [W_{SF} A_S]. \tag{99}$$

The first sum applies over l dislocation types with elastic energy per unit length W_E, core energy per unit length W_C, and line density per unit volume ρ_D. The second applies over p point defect types with formation energy W_F and number density per unit volume ς_V. The third applies over r kinds of stacking faults of energy per unit area W_{SF} and area per unit volume A_S. Volume change δv per length L of dislocation line is calculated as[22,74,75]

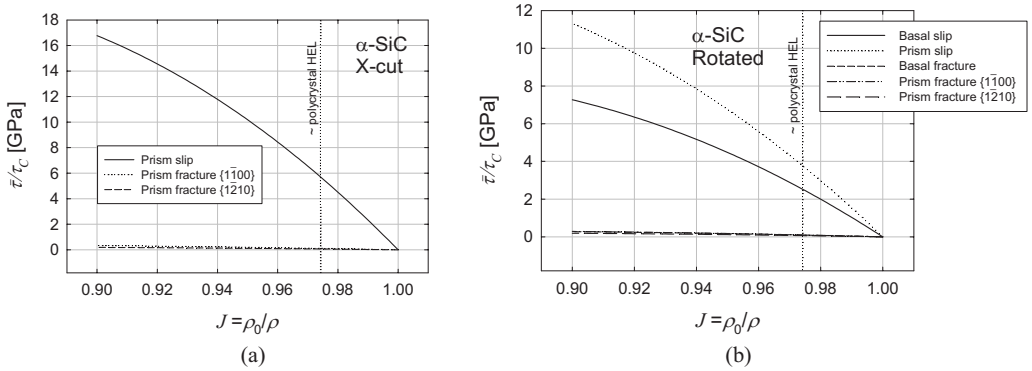

FIG. 8. Predicted ratio of resolved shear stress to critical shear stress for slip or shear fracture in α-SiC under voltage mode loading: (a) X-cut and (b) rotated cut. The values of τ_C listed in Table VII (Peierls barrier for slip) and Table IX (theoretical fracture strength). The strain at polycrystalline HEL is $\gamma \approx 0.024$ at $|T| \approx 11.5$ GPa in SiC–B (Ref. 37).

$$\delta v/L = \begin{cases} \frac{1}{3}\left[\frac{1-\nu-2\nu^2}{(1-\nu)B}(B'-1)+\frac{2-2\nu+2\nu^2}{(1-\nu)\mu}\left(\mu'-\frac{\mu}{B}\right)\right]W_E & \text{(edge dislocations)} \\ \frac{1}{\mu}\left(\mu'-\frac{\mu}{B}\right)W_E & \text{(screw dislocations)}, \end{cases} \tag{100}$$

where B' and μ' are pressure derivatives of bulk and shear moduli in Table II. Elastic and core energies and predicted volume changes per unit length of dislocation line are listed for 6*H*-SiC in Table X. For edge dislocations, the upper and lower bounds on B' are considered (Table II) in the calculation. Volume change for the 90° partial is computed from the first of (100) for a pure edge dislocation. Volume change for the edge loop is estimated[74] from the first of (100). An analytical elasticity solution for volume change from a mixed 60° dislocation is not available, so volume changes computed for both screw and edge dislocations are offered in Table X as bounds for the 60° dislocation. Core energies depend on the termination location of the core (C atom or Si atom) and are on the order of 10% of the elastic energy.[5] From Table X, the volume change from full dislocations depends little on B' or orientation (screw versus edge). Partial dislocations impart a significantly lower volume change ($\sim 1/3$ that of full dislocations) because of their lower line energy. Predicted volume changes are positive (dislocations cause expansion), as observed for a number of other materials,[74,77] and are comparable in magnitude to those predicted[22] in Al_2O_3. Dislocation density magnitudes $\rho_D \approx 10^{15}$ m^{-2} have been observed[2] in shock-loaded α-SiC, which for full dislocations corresponds to expansion of ~ 0.0003 and for partials expansion of ~ 0.0001. The former (0.03% volumetric expansion) would be offset by a pressure of ~ 0.07 GPa, implicitly affecting stress-strain responses. These predictions suggest that volume changes imparted by dislocations are small, but may warrant consideration in high fidelity equations of state for α-SiC constructed from the shock data.

TABLE X. Dislocation energies and predicted volume changes per unit defect length.

Dislocation	Elastic energy, W_E (nJ/m)[a]	Volume change per unit length, $\delta v/L$ (nm^2)	Nonlinear elasticity
Full 60°	21.1	0.278	$B'=4.0$
		0.233	$B'=2.5$
		0.275	$\mu'=2.5$ [b]
Edge loop	18.5	0.244	$B'=4.0$
		0.205	$B'=2.5$
Partial 90°	7.2	0.095	$B'=4.0$
		0.080	$B'=2.5$

[a]Reference 5.
[b]Screw dislocation; volume changes in all other rows assume edge dislocations.

Vacancy formation energies for missing C or Si atoms are listed Table XI, obtained from density functional theory (DFT) calculations[6] conducted elsewhere for conditions in which equal chemical potentials of C and Si atoms were specified. Equating the formation energy with the elastic energy of a spherical point defect in an infinite medium gives the following approximation for the relaxation volume of a vacancy,[73,86,87] negative in sign since the vacancy causes contraction of neighboring atoms toward the vacant site

$$\delta\Omega = -\bar{c}[(3\Omega_0 W_F)/(2\mu)]^{1/2}, \tag{101}$$

where $\bar{c}=3(1-\nu)/(1+\nu)$. The net volume change per vacancy defect is

$$\delta v = \Omega_0 + (1+\Xi)\delta\Omega, \quad \Xi = -[1/\bar{c}][\mu' - \mu/B] \times [2W_F/(3\mu\Omega_0)]^{1/2}. \tag{102}$$

In Eq. (102), atomic volume Ω_0 accounts for the displaced atom that formerly occupied the vacant site. Factor Ξ accounts for nonlinear elasticity.[73] While relaxation volume (101) is negative accounting for contraction of neighboring atoms toward the vacancy, total volume change (102) is positive in SiC, as shown in Table XI, because of the contribution of the displaced atom. From Table XI, volumetric expansion per 1 at. % of missing Si atoms is 0.0034 and per 1 at. % of missing C atoms is 0.0030. Relations (99), (100), and (102) combine to produce the residual volume change entering Eqs. (84) and (86) as follows:

$$\bar{J} = 1 + \sum_l [(\delta v/L)\rho_D] + \sum_p [(\delta v)\mathfrak{s}_V]. \tag{103}$$

VI. CONCLUSIONS

A model has been developed for electromechanical behavior of single crystals of 6*H*-SiC. The model has been used to predict the response of crystals of various orientations to planar shock loading under voltage mode and current mode electrical boundary conditions. Notable results are summarized as follows.

- Anisotropy and nonlinear elastic properties (i.e., third-

TABLE XI. Vacancy energies and predicted volume changes per defect.

Vacancy	Energy, W_F (eV)[a]	Relaxation volume, $\delta\Omega$ (Å^3)	Net volume change, δv (Å^3)
C	3.4	−14.28	3.11
Si	5.3	−17.83	3.53

[a]Reference 6.

order elastic constants or pressure derivatives of second-order elastic coefficients) can significantly affect the predicted axial stress for uniaxial compressive strains up to 0.1.
- Thermal expansion, piezoelectricity, and electrostriction have negligible effect on the predicted axial stress for uniaxial compressive strains up to 0.1.
- The choice of voltage mode or current mode boundary conditions has a negligible influence on the predicted axial stress so long as the material remains elastic.
- The displacement current produced during current mode loading of a Z-cut 6*H*-SiC specimen exceeds the displacement current produced in a shocked X-cut quartz specimen[23,68] of the same physical dimensions and subjected to the same axial strain.
- The electric field generated under current mode loading of a Z-cut 6*H*-SiC specimen would be sufficient to induce dielectric breakdown at strains greater than ~0.05, if the ambient breakdown field strength[67] applies at high pressures.
- Displacement currents predicted for current mode loading of Z-cut and rotated-cut 6*H*-SiC specimens at compressions near the polycrystalline HEL exceed magnitudes of injection current needed to lower the activation energy barrier for slip of partial dislocations under ambient conditions.[14]
- Shear stresses generated during shock loading of X-cut and rotated-cut specimens appear large enough to induce slip of basal and prism dislocations at strains corresponding to the polycrystalline HEL if the Peierls stress is an accurate measure of slip resistance. Shear stresses generated do not achieve the theoretical strength for fracture on basal or prism planes for compressive strains up to 0.1.
- Net volume changes associated with dislocation lines and vacancies are positive; i.e., defects cause expansion. Volume changes induced by dislocation line densities observed experimentally[2] would impart a small effect on the hydrostatic pressure.

The model developed here can be extended to provide a more detailed description of defects. Features not incorporated explicitly include drag stress proportional to dislocation velocity[79] and increasing strength with increasing defect density.[22,46] The effects of dislocation arrangement and velocity on stored energy in the defective crystal, important in metals deformed at extreme rates,[88,89] presumably are of importance in ceramic crystals deformed under similar conditions. The model may serve several purposes in the future. The model can be used in mesoscale simulations of shock-loaded polycrystals,[40–42,90,91] providing information on the grain-scale response of α-SiC. Model predictions can also provide insight into the relative importance of physical mechanisms incorporated in macroscopic constitutive models used in ballistics calculations.[92,93]

[1] J. Qian, L. L. Daemen, and Y. Zhao, Diamond Relat. Mater. **14**, 1669 (2005).
[2] T. B. Merala, H. W. Chan, D. G. Howitt, P. V. Kelsey, G. E. Korth, R. L. Williamson Mater. Sci. Eng., A **105–106**, 293 (1988).
[3] K. Kamitani, M. Grimsditch, J. C. Nipko, and C.-K. Loong, J. Appl. Phys. **82**, 3152 (1997).
[4] J. Zhang, L. Wang, D. J. Weidner, T. Uchida, and J. Xu, Am. Mineral. **87**, 1005 (2002).
[5] A. T. Blumenau, C. J. Fall, R. Jones, S. Oberg, T. Frauenheim, and P. R. Briddon, Phys. Rev. B **68**, 174108 (2003).
[6] N. Bernstein, H. J. Gotsis, D. A. Papaconstantopoulos, and M. J. Mehl, Phys. Rev. B **71**, 075203 (2005).
[7] R. W. G. Wyckoff, *Crystal Structures* (Wiley, New York, 1963), pp. 113–120.
[8] R. Feng, G. F. Raiser, and Y. M. Gupta, J. Appl. Phys. **79**, 1378 (1996).
[9] D. P. Dandekar, U.S. Army Research Laboratory Technical Report No. ARL-TR-2695, 2002.
[10] C. H. Shih, M. A. Meyers, V. F. Nesterenko, and S. J. Chen, Acta Mater. **48**, 2399 (2000).
[11] A. Qteish, V. Heine, and R. J. Needs, Physica B **185**, 366 (1993).
[12] S. Sugiyama and M. Togaya, J. Am. Ceram. Soc. **84**, 3013 (2001).
[13] T. J. Vogler, W. D. Reinhart, L. C. Chhabildas, and D. P. Dandekar, J. Appl. Phys. **99**, 023512 (2006).
[14] A. Galeckas, J. Linnros, and P. Pirouz, Appl. Phys. Lett. **81**, 883 (2002).
[15] T. A. G. Eberlein, R. Jones, A. T. Blumenau, S. Oberg, and P. R. Briddon, Phys. Status Solidi C **4**, 2923 (2007).
[16] A. V. Samant, W. L. Zhou, and P. Pirouz, Phys. Status Solidi A **166**, 155 (1998).
[17] J. L. Demenet, M. H. Hong, and P. Pirouz, Scr. Mater. **43**, 865 (2000).
[18] L. I. van Torne, Phys. Status Solidi **14**, K123 (1966).
[19] F. Gao and W. J. Weber, Philos. Mag. **85**, 509 (2005).
[20] H. Kitahara, Y. Noda, F. Yoshida, H. Nakashima, N. Shinohara, and H. Abe, J. Ceram. Soc. Jpn. **109**, 606 (2001).
[21] R. A. Graham and W. P. Brooks, J. Phys. Chem. Solids **32**, 2311 (1971).
[22] J. D. Clayton, Proc. R. Soc. London, Ser. A **465**, 307 (2009).
[23] R. A. Graham, Phys. Rev. B **6**, 4779 (1972).
[24] R. A. Graham, J. Appl. Phys. **48**, 2153 (1977).
[25] W. Ani and G. A. Maugin, J. Acoust. Soc. Am. **85**, 599 (1989).
[26] G. Arlt and G. R. Schodder, J. Acoust. Soc. Am. **37**, 384 (1965).
[27] S. Y. Davydov, Phys. Solid State **46**, 1200 (2004).
[28] G. A. Slack, J. Appl. Phys. **35**, 3460 (1964).
[29] L. Patrick and J. Choyke, Phys. Rev. B **2**, 2255 (1970).
[30] E. A. Burgemeister, W. Von Muench, and E. Pettenpaul, J. Appl. Phys. **50**, 5790 (1979).
[31] Z. Li and R. C. Bradt, J. Am. Ceram. Soc. **70**, 445 (1987).
[32] S. Karmann, R. Helbig, and R. A. Stein, J. Appl. Phys. **66**, 3922 (1989).
[33] K. Karch, P. Pavone, W. Windl, O. Schutt, and D. Strauch, Phys. Rev. B **50**, 17054 (1994).
[34] K. Karch, F. Bechstedt, P. Pavone, and D. Strauch, Phys. Rev. B **53**, 13400 (1996).
[35] A. P. Mirgorodsky, M. B. Smirnov, E. Abdelmounim, T. Merle, and P. E. Quintard, Phys. Rev. B **52**, 3993 (1995).
[36] M. Stockmeier, R. Muller, S. A. Sakwe, P. J. Wellmann, and A. Magerl, J. Appl. Phys. **105**, 033511 (2009).
[37] R. Feng, G. F. Raiser, and Y. M. Gupta, J. Appl. Phys. **83**, 79 (1998).
[38] S. Shim, J. Jang, and G. M. Pharr, Acta Mater. **56**, 3824 (2008).
[39] H.-P. Chen, R. K. Kalia, A. Nakano, P. Vashishta, and I. Szlufarska, J. Appl. Phys. **102**, 063514 (2007).
[40] D. Zhang, M. S. Wu, and R. Feng, Mech. Mater. **37**, 95 (2005).
[41] D. Zhang, M. S. Wu, and R. Feng, Int. J. Plast. **21**, 801 (2005).
[42] K. S. Zhang, D. Zhang, R. Feng, and M. S. Wu, J. Appl. Phys. **98**, 023505 (2005).
[43] G. A. Maugin, *Continuum Mechanics of Electromagnetic Solids* (North-Holland, Amsterdam, 1988), pp. 559–566.
[44] R. M. McMeeking, C. M. Landis, and S. M. A. Jimenez, Int. J. Non-Linear Mech. **42**, 831 (2007).
[45] J. D. Clayton, Int. J. Non-Linear Mech. **44**, 675 (2009).
[46] J. D. Clayton, J. Mech. Phys. Solids **53**, 261 (2005).
[47] J. D. Clayton, D. J. Bammann, and D. L. McDowell, Philos. Mag. **85**, 3983 (2005).
[48] J. D. Clayton, P. W. Chung, M. A. Grinfeld, and W. D. Nothwang, Int. J. Eng. Sci. **46**, 10 (2008).
[49] P. J. Chen, M. F. McCarthy, and T. R. O'Leary, Arch. Ration. Mech. Anal. **62**, 189 (1976).
[50] R. N. Thurston, in *Handbuch der Physik VIa4*, edited by C. Truesdell (Springer-Verlag, Berlin, 1971), pp. 109–308.
[51] M. Lax and D. F. Nelson, Phys. Rev. B **13**, 1777 (1976).
[52] R. A. Toupin, Ind. Univ. Math. J. **5**, 849 (1956).

[53]H. F. Tiersten, Int. J. Eng. Sci. **9**, 587 (1971).
[54]W. L. Bond *et al.*, Proc. IRE **37**, 1378 (1949).
[55]B. D. Coleman and W. Noll, Arch. Ration. Mech. Anal. **13**, 167 (1963).
[56]Z. Li and R. C. Bradt, in *Ceramic Transactions: Silicon Carbide '87*, edited by J. D. Cawley and C. E. Semler (American Ceramic Society, Westerville, OH, 1989), pp. 313–339.
[57]P. N. Keating, Phys. Rev. **145**, 637 (1966).
[58]A. Polian, J. M. Besson, M. Grimsditch, and H. Vogt, Phys. Rev. B **25**, 2767 (1982).
[59]W. A. Bassett, M. S. Weathers, T.-C. Wu, and T. Holmquist, J. Appl. Phys. **74**, 3824 (1993).
[60]T. Sekine and T. Kobayashi, Phys. Rev. B **55**, 8034 (1997).
[61]J. C. Slater, *Introduction to Chemical Physics* (McGraw-Hill, New York, 1939), pp. 238–240.
[62]R. D. Mindlin, J. Elast. **2**, 217 (1972).
[63]S. G. Müller, R. Eckstein, J. Fricke, D. Hofmann, R. Hofmann, R. Horn, H. Mehling, and O. Nilsson, Mater. Sci. Forum **264–268**, 623 (1998).
[64]O. M. Stuetzer, J. Appl. Phys. **38**, 3901 (1967).
[65]R. A. Graham and W. J. Halpin, J. Appl. Phys. **39**, 5077 (1968).
[66]R. A. Graham and G. E. Ingram, J. Appl. Phys. **43**, 826 (1972).
[67]R. Singh, Microelectron. Reliab. **46**, 713 (2006).
[68]R. A. Graham, F. W. Neilson, and W. B. Benedick, J. Appl. Phys. **36**, 1775 (1965).
[69]R. Brugger, J. Appl. Phys. **36**, 759 (1965).
[70]G. Yuan, R. Feng, and Y. M. Gupta, J. Appl. Phys. **89**, 5372 (2001).
[71]G. M. Amulele, M. H. Manghnani, B. Li, D. J. H. Errandonea, M. Somayazulu, and Y. Meng, J. Appl. Phys. **95**, 1806 (2004).
[72]M. E. Kipp and D. E. Grady, Sandia Laboratories Report No. SAND89-1461-UC-704, 1989.
[73]J. D. Eshelby, J. Appl. Phys. **25**, 255 (1954).
[74]J. Holder and A. V. Granato, Phys. Rev. **182**, 729 (1969).
[75]A. Seeger and P. Haasen, Philos. Mag. **3**, 470 (1958).
[76]R. A. Toupin and R. S. Rivlin, J. Math. Phys. **1**, 8 (1960).
[77]T. W. Wright, Mech. Mater. **1**, 185 (1982).
[78]E. H. Lee and D. T. Liu, J. Appl. Phys. **38**, 19 (1967).
[79]U. F. Kocks, A. S. Argon, and M. F. Ashby, Prog. Mater. Sci. **19**, 1 (1975).
[80]K. Maeda, S. Suzuki, M. Fujita, M. Ishihara, and S. Hyodo, Philos. Mag. A **57**, 573 (1988).
[81]J. P. Hirth and J. Lothe, *Theory of Dislocations* (Wiley, New York, 1982), pp. 838–839.
[82]F. R. N. Nabarro, Proc. Phys. Soc. London **59**, 256 (1947).
[83]A. J. E. Foreman, Acta Metall. **3**, 322 (1955).
[84]Y. A. Farber, S. Y. Yoon, K. P. D. Lagerlof, and A. H. Heuer, Phys. Status Solidi A **137**, 485 (1993).
[85]J. Frenkel, Z. Phys. **37**, 572 (1926).
[86]F. Bitter, Phys. Rev. **37**, 1527 (1931).
[87]C. Teodosiu, *Elastic Models of Crystal Defects* (Springer-Verlag, Berlin, 1982), pp. 287–295.
[88]A. Zubelewicz, P. J. Maudlin, G. T. Gray III, and A. K. Zurek, Phys. Rev. B **71**, 104107 (2005).
[89]A. Zubelewicz, Phys. Rev. B **77**, 214111 (2008).
[90]S. K. Dwivedi, J. R. Asay, and Y. M. Gupta, J. Appl. Phys. **100**, 083509 (2006).
[91]T. J. Vogler and J. D. Clayton, J. Mech. Phys. Solids **56**, 297 (2008).
[92]A. M. Rajendran and D. J. Grove, Int. J. Impact Eng. **18**, 611 (1996).
[93]T. J. Holmquist and G. R. Johnson, J. Appl. Phys. **91**, 5858 (2002).

NO. OF
COPIES ORGANIZATION

1 (PDF ONLY) DEFENSE TECHNICAL INFORMATION CTR
DTIC OCA
8725 JOHN J KINGMAN RD
STE 0944
FORT BELVOIR VA 22060-6218

1 DIRECTOR
US ARMY RESEARCH LAB
IMNE ALC HRR
2800 POWDER MILL RD
ADELPHI MD 20783-1197

1 DIRECTOR
US ARMY RESEARCH LAB
RDRL CIM L
2800 POWDER MILL RD
ADELPHI MD 20783-1197

1 DIRECTOR
US ARMY RESEARCH LAB
RDRL CIM P
2800 POWDER MILL RD
ADELPHI MD 20783-1197

ABERDEEN PROVING GROUND

1 DIR USARL
RDRL CIM G (BLDG 4600)

NO. OF
COPIES ORGANIZATION

1 DIRECTOR
US ARMY RSRCH LAB
RDRL SER L
W NOTHWANG
ADELPHI MD 20783-1197

ABERDEEN PROVING GROUND

57 DIR USARL
RDRL CI
R NAMBURU
RDRL CIH C
P CHUNG
J KNAP
D GROVE
RDRL SL
R COATES
RDRL WM
J MCCAULEY
B FORCH
S KARNA
RDRL WML H
T FARRAND
M FERMEN-COKER
C MEYER
S SCHRAML
B SCHUSTER
RDRL WMM B
B CHEESMAN
G GAZONAS
C RANDOW
C F YEN
RDRL WMM E
M COLE
RDRL WMM G
J ANDZELM
RDRL WMP
S SCHOENFELD
RDRL WMP B
R BECKER
S BILYK
D CASEM
D DANDEKAR
M GREENFIELD
C HOPPEL
J HOUSKAMP
Y HUANG
R KRAFT
B LEAVY
B LOVE
M RAFTENBERG
M SCHEIDLER

NO. OF
COPIES ORGANIZATION

T WEERASOORIYA
K ZIEGLER
C WILLIAMS
RDRL WMP C
T BJERKE
S SEGLETES
W WALTERS
RDRL WMP D
R DONEY
RDRL WMP F
N GNIAZDOWSKI
RDRL WM S
T JONES
RDRL WMT D
J CLAYTON (15 CPS)